Article:

Anthonissen, C.J., Leon, L.A., Wolfe, F.D. et al. (2026) Structural evolution and slip rate variations through time of the Puente Hills blind-thrust fault beneath Los Angeles: Implications for seismic hazard and folding kinematics. Journal of Geophysical Research: Solid Earth, 131 (6). e2025JB032405. ISSN: 2169-9313

https://doi.org/10.1029/2025jb032405

Structural evolution and slip rate variations through time of the Puente-Hills blind-thrust beneath Los Angeles: Implications for seismic hazard and folding kinematics

Authors

C.J. Anthonissen[1], L.A. Leon[1], F.D. Wolfe[2], J. Don[2], J.F. Dolan[1], J.H. Shaw[2], T.L. Pratt[3], E.J. Rhodes[4], T.M. Rittenour[5], A. Ivester[4]

[1] Department of Earth Sciences, University of Southern California, Los Angeles, CA, USA

[2] Department of Earth and Planetary Sciences, Harvard University, Cambridge, MA, USA

[3] U.S. Geological Survey, Reston, VA, USA

[4] School of Geography and Planning, University of Sheffield, Sheffield, UK

[5] Department of Geosciences, Utah State University, Logan, UT, USA

Key Points

- We constrain a 1.4 My incremental slip history for the Puente Hills blind-thrust fault (PHT), revealing variable rates from as slow as 0.16 mm/yr to as fast as 2.5 mm/yr.
- Forelimb folding records < 80% of the slip accommodated on the deep fault ramp. Thus, forelimb strata may underestimate total fault slip.
- A significant increase in slip rate after ~200 ka matches timing of acceleration on the adjacent Los Angeles segment, indicating a kinematic linkage.

Abstract

Using seismic reflection profiles, historical well logging data, and luminescence and radiocarbon ages, we determine a Pleistocene-Holocene slip history for the central, Santa Fe Springs segment of the Puente Hills blind-thrust fault (PHT), a major seismogenic fault situated beneath the urbanized Los Angeles metropolitan region. We analyze the geometry of correlative stratigraphic units in the forelimb and backlimb of the overlying growth-fold, the Santa Fe Springs anticline, and determine the uplift of seven age-correlative markers. Uplift measurements are converted to thrust displacements on the underlying PHT using a structural method laid out by Don et al. (2022) that accounts for the geometry of the fault. These data indicate that deep thrust displacement on the PHT is partially consumed updip in the creation of a hanging-wall fault-bend fold, with forelimb growth strata recording < 80% of the slip documented within the backlimb. Chronological data from growth strata yield age constraints for folding and faulting on the underlying PHT, providing a detailed incremental slip history derived from both the forelimb and backlimb folding for seven discrete growth horizons, spanning the past 1.4 million years. The resulting six incremental slip rates demonstrate that fault slip has varied through time from the middle Pleistocene to the Holocene. Moreover, these results reveal synchronous acceleration of both the central, Santa Fe Springs and western, Los Angeles segments of the fault system since late Pleistocene time (after 200 ka) and slip rates of greater than 2 mm/yr on the downdip, backlimb, fault-ramp below the anticline.

Plain Language Summary:

We studied the earthquake history of the Puente Hills blind-thrust fault (PHT), a major seismic source buried directly beneath metropolitan Los Angeles. Using a combination of underground imaging datasets—including seismic reflection profiles and drilling data—we mapped and dated time-correlative sedimentary layers that record deformation caused by movement on the fault beneath. By comparing patterns of folding across the structure above the PHT, we show that cumulative slip is greater on deeper

parts of the fault than on shallower segments. This indicates that shallow sub-surface evidence may underestimate the total amount of fault movement. We also developed a long-term slip history spanning approximately 1.4 million years, revealing that the fault system became increasingly active sometime after about 200,000 years ago. These findings help improve our understanding of how blind-thrust faults evolve and accommodate strain over time and may be used to refine earthquake hazard models in places like Los Angeles.

1. Introduction

The Puente Hills blind-thrust fault (PHT) is a north-dipping thrust system that extends west northwest-south southeast for more than 40 km beneath the northern half of the Los Angeles metropolitan area in Southern California (Figure 1; Shaw et al., 2002). Given its large surface area, complex geometry, and location beneath one of the most densely populated urban centers in the United States, the PHT represents one of the largest seismic hazards in the country (Shaw et al., 2002; Field et al., 2005).

Unlike surface-rupturing faults, blind thrust faults such as the PHT accommodate deformation in the upper few kilometers of the crust through fold growth above the buried fault tip (Suppe et al., 1992; Shaw & Suppe, 1996). These growth folds record incremental deformation and provide a critical means of investigating recent fault activity and constraining the history of past earthquakes. Seismic reflection data, drilling records, and earthquake data from across the Los Angeles Basin reveal that the PHT is an active fault system composed of three moderately north-dipping fault segments, each buried several kilometers below the surface and overlain by growth folds (Shaw & Shearer, 1999; Pratt et al., 2002; Shaw et al., 2002; Dolan et al., 2003). Furthermore, analyses of these data indicate that a complete rupture of the PHT could generate an earthquake of $M_w > 7$ directly beneath Los Angeles, posing a significant risk to the region (Dolan et al., 2003, Leon et al., 2007). The key to understanding the seismic hazard posed by the PHT lies in documenting the rate at which it stores and releases seismic energy through time. Recent studies such as those by Gauriau & Dolan (2021, 2024) indicate that strike-slip faults within complex plate boundary systems, like those bounding the Los Angeles Basin, exhibit variable rates of strain accumulation and release over timescales spanning multiple earthquake cycles and several tens of meters of fault slip. Capturing these temporally variable patterns of strain release therefore requires detailed incremental slip rate records at multiple time scales averaged over different time and displacement intervals.

In this study, we integrate high-resolution seismic reflection data, drilling logs, and geochronological data, including radiocarbon (^{14}C) dating to reconstruct the Pleistocene-Holocene slip history of the central Santa Fe Springs segment of the PHT. By analyzing seven folded, regionally continuous sedimentary marker horizons, we document incremental deformation spanning the past ~1400 kyr. We quantify both forelimb and backlimb fold growth and, using fault-bend folding theory (Suppe, 1983), we establish a relationship between deformation and fault slip across the entire fold, allowing us to determine incremental slip rates along different downdip sections of the fault. This approach provides new insights into long-term variations in fault slip rates, revealing temporal patterns of acceleration and deceleration on the fault. We integrate these new observations with slip-rate data from the Los Angeles segment of the PHT and other faults in the region and discuss these results in the context of the structural evolution of the PHT and the broader implications for seismic hazard assessment in the Los Angeles Basin.

2. Geologic Setting

The Los Angeles Basin is a northwest-southeast-elongate trough filled by a sequence of Miocene to Quaternary marine and terrigenous sediments that record a complex depositional and structural history dating back approximately 23 million years (Yerkes et al., 1965; Blake, 1991; Wright, 1991). Around 4 million years ago, a significant tectonic shift from an extensional to a compressional regime initiated ongoing north-south-directed shortening of the basin (Wright, 1991). Basin shortening is accommodated by a combination of near-vertical southeast-striking dextral strike-slip faults (e.g., Whittier, Newport-

Inglewood, Palos Verdes), east-striking sinistral strike-slip and oblique-reverse faults (e.g., Raymond, Hollywood, Santa Monica) and moderately north- and south-dipping, east- and southeast-striking thrust faults (e.g., Compton, Elysian Park, Wilmington), including the Puente Hills blind-thrust fault (PHT) (Figure 1; Hauksson, 1990; Wright, 1991; Dolan et al., 1995; Shaw & Suppe, 1996; Walls et al., 1998; Shaw & Shearer, 1999; Shaw et al., 2002; Argus et al., 2005; Dolan et al., 2007).

Geodetic data indicate that as much as 9 mm/yr of north-south shortening is currently being accommodated by elastic strain accumulation on these faults, with as much as 3 mm/yr attributed specifically to the PHT (Rollins et al., 2018). Previous geologic studies, however, have suggested that long-term slip rates on the basin's blind-thrust faults, including the PHT (0.6 - 1.7 mm/yr; - Shaw & Shearer, 1999; Dolan et al., 2003; Leon et al., 2007), the Compton blind-thrust fault (~1.2 mm/yr; - Leon et al., 2009), the Wilmington thrust (~0.16 mm/yr - Wolfe et al., 2019), and the Elysian Park thrust (~1.7 mm/yr; - Davis et al., 1989; Shaw and Suppe, 1996) are slower than these present-day rates of elastic strain accumulation (Dolan et al., 1995; Rollins et al., 2018). This strain accumulation/strain release rate discrepancy highlights the complexity of the basin's tectonic processes and has been cited as evidence that a significant seismic moment deficit may be accumulating in and around the Los Angeles area (Dolan et al., 1995; Walls et al., 1998).

Figure 1 a.) The Puente Hills blind-thrust fault (PHT) is a west-northwest to east-southeast trending blind thrust fault which extends for ~40 km from downtown Los Angeles in the northwest to Fullerton in the southeast. Three, north-dipping, buried, en-echelon fault segments comprise the PHT. These are, from west-northwest to east-southeast the Los Angeles segment, the Santa Fe Springs segment, and the Coyote Hills segment. The position and geometries of these segments, which terminate at a depth of ~3 km, were constrained by extensive drilling and seismic reflection data (Shaw et al., 2002). Blue lines on the fault surfaces are depth contours at 2000 m intervals, with the shallowest contour on each surface located at - 4000 m ASL. Fault traces shown in the figure are from the Statewide California Earthquake Center (SCEC) Community Fault Model (CFM 5.2; Plesch et al., 2007). PVF = Palos

Verdes fault; CF = Compton fault; NIF = Newport-Inglewood fault, SMF = Santa Monica fault; HF = Hollywood fault; VF = Verdugo fault; EPF = Upper Elysian Park fault; WF = Whittier fault; CHNF = Chino fault; SJF = San Jose fault; CCF = Cucamonga fault; SMAF = Sierra Madre fault. b.) Reference map showing the spatial distribution of the datasets used in this study. The forelimb and backlimb fold axial traces of the Santa Fe Springs anticline are shown as green dashed lines. Drill datasets are shown as crosses, except for the Pico Rivera hole which is shown as a white circle with a black dot. The seismic reflection profiles are shown in purple (industry reflection profile) and blue (high resolution backlimb seismic reflection profile). CADPW = California Department of Public Works.

2.1. The Puente Hills Blind-Thrust Fault (PHT)

The PHT was first identified by Shaw and Shearer (1999) through the analysis of seismic reflection data, petroleum well logs, and relocation of the 1987 M_w = 5.9 Whittier Narrows earthquake and aftershocks. The PHT consists of three north-dipping, *en echelon* fault segments: from west to east, the Los Angeles, Santa Fe Springs, and Coyote Hills segments (Shaw et al., 2002; Pratt et al., 2002). The central Santa Fe Springs segment, which is the focus of this study, dips approximately 27° (across most of the fault's downdip extent) to the north-northeast. The thrust ramp extends upward to a depth of about 3 km beneath the Santa Fe Springs anticline (SFSA) —a broad fold that is thought to have developed, initially, during Pliocene time through fault-propagation folding processes but has experienced a more recent history during which it has developed as a fault-bend fold (Figure 2; Allmendinger & Shaw, 2000; Shaw et al., 2002).

Dolan et al. (2003) and Leon et al. (2007) found evidence for at least three Holocene earthquakes in growth strata above the forelimb of the Santa Fe Springs anticline. Their measurements of paleo-fold scarp heights indicate that these scarps were generated by large-magnitude earthquakes ranging from M_w 7.2 to 7.5. Detailed stratigraphic analyses indicate that these three earthquakes occurred within the past ~8100 years, with the most recent earthquake occurring after 3000 years ago and prior to 1780 C.E. (Leon et al., 2007).

Figure 2. Industry seismic reflection profile and schematic cross section showing the Santa Fe Springs anticline (SFSA) and PHT fault, modified after data and interpretations in Shaw & Shearer (1999). **The seismic data do not resolve stratigraphy in the upper ~200 m below the ground surface.** ***This figure highlights three fault ramp segments (BLR-S1 = Backlimb thrust ramp S1, and BLR-S2 = Backlimb thrust ramp S2, FLR = Forelimb thrust ramp). Deformation is localized within north- and south-dipping kink bands bounded by axial surfaces that project to bends in the underlying fault, consistent with a fault-bend fold geometry. Upward-narrowing growth triangles in the Quaternary section indicate syntectonic deposition, with fold growth by kink band formation initiating during the Pliocene on the backlimb. Moderately north-dipping discontinuous reflectors image the forelimb fault ramp, whereas downdip, backlimb, ramp geometry is constrained by fault-bend folding models and relocated aftershocks of the 1987 Mw 5.9 Whittier Narrows earthquake. The pink dashed line marks the inferred trace of a fault (interpreted as a backthrust) intersected by two petroleum industry wells. However, the seismic reflection data show no evidence for significant displacement along this structure. Qt = Quaternary; Plio = Pliocene; Tfu = upper Fernando Formation; Tfl = lower Fernando Formation; Tp = Miocene Puente Formation***

3. Observations of folding above the Puente Hills blind-thrust fault (PHT)

3.1. Subsurface data used to constrain folding and chronology

We utilized seismic reflection profiles, borehole data, and subsurface mapping based on well logs to: (1) constrain the geometry of the fault plane and the overlying growth folding above the Santa Fe Springs segment of the PHT; (2) determine the depositional ages of syntectonic growth strata; and (3) calculate rates of thrust displacement through time. Seismic reflection data at multiple scales provide two-dimensional profiles of the fault and associated growth fold, and drilling data enable cross-fold correlations of sedimentary growth strata in the forelimb and backlimb, providing temporal constraints on fold growth while also verifying depth migrations of the seismic reflection data. Furthermore, shallow drill hole observations within the upper ~50 m of the subsurface were corroborated with subsurface mapping from the California Department of Water Resources (CDWR, 1961). Figure 1b shows the spatial distribution of all datasets employed in this study, while detailed descriptions of each dataset are provided in section 1 of the *Supplemental Materials*.

Specifically, four seismic reflection profiles were utilized to constrain geometric parameters of fault-related folding and quantify the deformation of stratigraphy. These are: a deep-penetration, regional-scale petroleum industry seismic reflection profile – the same seismic reflection data analyzed by Shaw et al. (2002) - and; three relatively short-length shallow seismic reflection profiles collected above the zones of forelimb and backlimb folding (Figure 1b and Figure 4; *Supplemental Figures S1A and S1B; Pratt et al. 2002*).

To constrain the stratigraphy of the SFSA and establish the depositional ages of deformed marker horizons, we use four different sets of borehole data, including (1) a 65.75-m-deep, continuously cored borehole drilled into the backlimb of the SFSA, hereafter referred to as the Pico Rivera borehole; (2) a transect of closely spaced, continuously cored boreholes and Cone Penetrometer Test holes (CPTs), drilled across the forelimb growth triangle; (3) a regional network of geotechnical boreholes drilled by The California Department of Public Works (CADPW) (https://maps.conservation.ca.gov/cgs/informationwarehouse/bhdb/); and (4) a set of water monitoring wells drilled by the U.S. Geological Survey (USGS) into the SFSA (Land et al., 2004).

Seven marker horizons corresponding to the tops of distinct stratigraphic units delineated in the drilling data serve as numerical age markers for late Pleistocene deformation, enabling us to establish a robust temporal framework for long-term tectonic activity on the Santa Fe Springs segment of the PHT. Depositional ages are drawn from regional studies of the sedimentary development of the Los Angeles Basin (Ponti et al., 2014; McDougall et al., 2012; Ponti et al., 2007; Leon et al., 2007; Dolan et al., 2003), supplemented by four radiocarbon (^{14}C) dates and 21 luminescence dates from samples in the Pico Rivera borehole on the backlimb of the SFSA.

3.2. Relationship between fault displacement and fold growth

Shaw et al. (2002) identified the anticlinal fold above the Santa Fe Springs segment of the Puente Hills blind-thrust fault (PHT) as a fault-bend fold, formed during thrust displacement on the underlying fault plane during middle Pleistocene-Holocene time. We apply fault-bend folding theory (Suppe, 1983) to calculate fault displacements over time, through investigation of the age and geometry of shallow folding and compile an incremental slip-rate record for the PHT. Fault-bend folding theory posits that sedimentary layers maintain continuous length and constant orthogonal thickness as they fold above changes in dip on the underlying thrust fault (Figure 3; Suppe, 1983; Shaw et al., 1994; Shaw et al., 2004; Connors et al., 2021). In compressional settings experiencing sedimentation, discrete axial fold surfaces bound a kink band that forms an upward-narrowing growth triangle. The width of the kink band and the structural relief of strata within it decrease upward, toward the surface, as progressively younger strata are transported across a fault-bend during thrust displacement, forming a distinct growth triangle (Figure 3).

As observed from the seismic reflection data shown in figure 2, the forelimb kink band is pinned to the tip line of the PHT thrust at a depth of ~3km, whereas the backlimb kink band is pinned to a steepened ramp section at a depth of ~6 km (Shaw et al., 2002). Syntectonic growth sediments from the Los Angeles and San Gabriel Rivers deposited onto the anticline appear as laterally continuous reflectors, showing a distinct decrease in structural relief and an upward narrowing of both the forelimb and backlimb kink band widths towards the surface. These growth sediments record fault activity, and we specifically analyze the deformation of marker horizons of known age crossing both the forelimb and backlimb growth triangles to determine the size and age of displacements on the underlying fault (Figure 3).

Similar methodologies have been effectively used in other studies to derive slip-rates and identify paleo-earthquakes in analogous geological settings (e.g., Medwedeff, 1992; Mueller & Suppe, 1997; Dolan et al., 2003; Benesh et al., 2007; Leon et al., 2007; McAuliffe et al., 2015; Bergen et al., 2017). We measured the dips of axial surfaces, changes in dip of strata across the kink bands, and the widths and structural relief of the kink bands to constrain the structural parameters of the fault-bend fold system and calculate displacements on the underlying fault (Section 5 of the *Supplemental materials, Table S3 and S4*).

Figure 3. Schematic illustration of the fault-bend folding mechanisms operating on the Santa Fe Springs anticline. a.) The top figure shows the position of the forelimb (FLR) and backlimb kink bands (BLR-S1 and BLR-S2) on the industry seismic reflection profile. b.) Forelimb kink band formation results from material displaced upwards and horizontally over the fault tip. Displacement at the tip (S) equals the uplift of growth strata (U) divided by the sine of the fault dip (α). c.) Backlimb kink band and associated growth triangle form in response to displacement through a deeper bend in the fault. Displacements through the bend (S_1 and S_2) govern the uplift of strata on either side of the kink band and depend on the changes in dip (α_1 and α_2) between ramp segments. Variables U_T and U_1 (in red) cannot be directly measured from the seismic reflection profiles.

3.3. Determining the shape of the fault and the fold

The active anticlinal axial surface of the forelimb kink band is pinned to the fault tip (at ~3 km depth) as directly observed and measured on the industry seismic reflection profile. In contrast, the active synclinal axial surface of the backlimb kink band is pinned to a change in dip of the fault plane at a depth of ~6 km (Figure 2, Figure 4, and *Supplemental Figure S7)*. While the fault plane is clearly imaged in the shallowest portion of the industry seismic reflection profile, it is poorly resolved at depths below 4 km, and the change in dip is not directly imaged. As this change in dip is not well-imaged, we apply fault-bend folding theory to calculate the change in dip at the pinning point of the backlimb synclinal axial surface (Section 4 of the *Supplemental Materials*). Our calculations indicate that the deep ramp steepens from ~27° to ~41° at the backlimb fault-bend. To simplify descriptions of these fault sections, we assign each an unique designation: (1) the ramp from the base of the forelimb ramp down the to the steepened backlimb ramp section is FLR, with a dip of 27°; (2) the steepened ramp downdip beneath the backlimb is BLR-S2, with a dip of 41°; and (3) the ramp further downdip to the north below the steepened ramp section is BLR-S1, with a dip of 27° (Section 4 of the *Supplemental materials*). Fault dips were measured on the time-migrated seismic reflection data that were converted to depth using three basin velocity models (slow, fast, and an intermediate preferred model). Different velocity models introduce a systematic uncertainty of ± 2° for all fault sections, with slower velocities yielding shallower apparent dips and faster velocities yielding steeper dips; the implications of these dip uncertainties are discussed in Section 3.5.3.

3.4. Determining the timing and size of incremental fault displacements

3.4.1. Age constraints of stratigraphic sequences

We used the seven stratigraphic sequences that were mapped throughout the subsurface of the Los Angeles Basin, and identified by us in the drilling datasets, to determine the long-term fold-growth history above the PHT from middle Pleistocene time to the present (Section 2 of the *Supplemental Materials)*. Ponti et al. (2007) first established this sequence stratigraphic framework through their analysis of drilling data, seismic reflection profiles, and chronostratigraphic datasets, identifying age-equivalent sedimentary sequences around the Long Beach area in the southern Los Angeles Basin. Later studies by Edwards et al. (2009), McDougall et al. (2012), Ponti et al. (2014), and Bergen (2015) extended this framework basin-wide, refining both the depositional ages and spatial extents of these sequences. These sequences record changes in depositional environments within the basin that were associated with base-level and paleoclimatic changes during late Pleistocene and Holocene time. Ages were determined using macro- and microfossil data, paleomagnetic correlations, marine oxygen isotope records, amino acid racemization dating, correlation of volcanic ash deposits, ^{14}C-dating, and luminescence-dating (McDougall et al., 2012; Ponti et al., 2014). Ponti et al. (2007, 2014) and Bergen (2015) mapped the upper contacts of these sequences in the water wells drilled by the U.S. Geological Survey. Specifically, three of these deep wells, Pico-2, Norwalk-2, and Cerritos-2, intersect the industry seismic reflection profile crossing the SFSA, allowing correlation between well data and seismic reflectors that represent the upper contacts of these sequences (Figure 4).

The depositional age of the top of each stratigraphic sequence is estimated based on the age ranges of the sequences directly above and below it, with the resulting age probability distributions dependent on the quality of chronological constraints available for these bounding sequences (Section 2 of the *Supplemental Materials*).

The stratigraphic sequences used for this study are, from youngest to oldest, the Dominquez, Mesa, Pacific, Harbor, upper Wilmington, lower Wilmington, and upper Long Beach, using the nomenclature first established by Ponti et al. (2007) and refined by McDougall et al. (2012) (Table 1, *Supplemental Table S1*). The Bent Spring and Pacific A sequences of Ponti et al. (2014) are absent in the study area.

In the study area, the top of the Dominguez sequence aligns with the current ground surface and thus cannot be effectively used as a stratigraphic marker. Instead, we utilize the top of the Gaspur aquifer as the shallowest marker unit. The Gaspur aquifer is the basal stratigraphic member of the Dominguez sequence and consists of a regionally extensive, laterally continuous layer of coarse-grained sand and gravel that is readily identified in the geotechnical drilling dataset described in this study. As the shallowest mappable and deformed unit with a well-established depositional age, the Gaspur aquifer provides a reliable measure of early Holocene to present deformation across the SFSA.

To constrain the age of the shallowest stratigraphy to a depth of 65 m, four charcoal samples and 21 luminescence samples were collected from the Pico Rivera borehole on the backlimb of the SFSA (Figure 4). Only one charcoal sample was large enough to provide a useful ^{14}C age, yielding an OxCal v.3.1 (Ramsey, 1995, 2001) calibrated age of ~21.36 - 13.52 ka from a silt layer at 35.4 m depth, directly beneath a relatively thick interval of homogeneous medium- and coarse-grained sands. This silt layer corresponds to the top of the Mesa sequence of Ponti et al. (2014), just below the coarse-grained Gaspur aquifer

(Figure 5). Luminescence samples were initially sent for quartz Optically Stimulated Luminescence (OSL) dating and subsequently for K-feldspar Infrared Stimulated Luminescence (IRSL) dating. Luminescence ages from both the OSL and IRSL studies, however, yielded inconsistent results, showing significant age fluctuations downhole, preventing us from compiling these into a reliable age model (Section 3 of the *Supplemental Materials*). Despite these inconsistencies, both luminescence datasets indicate a sharp increase in ages of several thousand years over a short depth interval approximately 4 m long at a depth of ~62 m. This abrupt increase in age supports the extrapolated position of the unconformable contact between the Pacific sequence (MIS 5e and 5c) and the underlying Harbor sequence (MIS 6 and older), as defined by Ponti et al. (2009) and McDougall et al. (2012) (Figure 4 - Inset). Radiocarbon ages on detrital charcoal samples from the study on the forelimb of SFSA by Dolan et al. (2003) and Leon et al. (2007) were used to constrain the age of the top of the Gaspur aquifer to between ~10.7 and 9.6 ka (Table 1, *Supplemental Table S1*).

Table 1. Structural relief and ages of marker horizons

3.4.2. Deformation of stratigraphic sequences

Using water-well drilling logs and three-dimensional (3D) models from Paulinsky et al. (2023) and Ponti et al. (2014), water-well logs from the Water Replenishment District (https://www.wrd.org/), and seismic reflection profile interpretations from Bergen (2015), we identified the tops of the Gaspur aquifer, and the Mesa, Pacific, Harbor, upper Wilmington, lower Wilmington, and upper Long Beach sequences (Figure 4 and Figure 5).

By measuring the uplift of each marker horizon, we compiled a record of incremental deformation on the forelimb and backlimb of the SFSA over the past ~1.4 Ma (Table 1). The top of each sequence is considered to represent the time between its deposition and that of the overlying sequence. The depositional ages used in this study (Table 1) closely align with those of Bergen et al. (2017), who estimated ages based on the deposition of entire units rather than the tops of the stratigraphic sequences that record the youngest possible age of deposition (*Supplemental Table S1*).

We measure slip on the PHT beneath the Santa Fe Springs anticline that has been accommodated by fold growth within the forelimb and backlimb kink bands. Slip estimates derived from uplift within the growth triangles assume ideal fault-bend folding behavior; however, mechanical modeling of growth fault-bend folds demonstrates that some internal deformation and compaction may be unaccounted for and can cause structural relief to slightly underestimate true fault slip (Benesh et al., 2007). Consequently, the slip magnitudes and rates reported here should be regarded as inherently conservative, as any shortening accommodated by distributed deformation or compaction outside the kink-band framework is not included.

To evaluate whether deformation outside the kink bands could bias our uplift-based slip estimates, we performed a line-length balance of a middle Pleistocene seismic reflector near the growth–to–pre-growth transition, that can be traced continuously across the entire SFSA (yellow highlighted seismic reflector no. 3 in Figure 2). Line-length balancing estimates horizontal shortening by comparing the restored length of a folded horizon to its present horizontal extent. This analysis shows that almost all displacement is recorded by shortening within the forelimb and backlimb kink bands, with only ~48 m of shortening accommodated between the kink bands over a north–south distance of ~6.2 km. Relative to the total fault slip of > 500 m inferred from kink-band width and uplift geometry of middle Pleistocene, distributed shortening between the kink bands thus represents no more than ~10% of cumulative fault slip since middle Pleistocene time, implying that any bias from distributed internal deformation is modest and that our uplift-derived slip estimates are conservative.

An additional consideration is that the high-resolution seismic reflection profile on the backlimb, together with data from the Pico Rivera borehole, reveals evidence for either erosion of the top of the Mesa or significantly reduced sediment accumulation on the upthrown side of the fold during this period. Because either process would diminish the apparent structural relief across the fold, this reinforces the interpretation described below that our slip-rate estimates are minimum values. In contrast, structural relief of the top of the Gaspur aquifer across the backlimb is based on boreholes near the eastern margin of the San Gabriel River channel, where fluvial incision is expected to have been minimal (Figure 5). While minor erosion of uplifted markers cannot be excluded, any such modification of the backlimb fold would likely reduce relief and thus would not challenge the conclusion that the reported slip rates are minimum estimates.

Figure 4. Correlation of stratigraphic sequences across the Santa Fe Springs anticline using industry and high-resolution seismic reflection profiles (inset), and borehole data. Sequence tops are matched to continuous reflectors traceable across the anticline flanks, though shallow reflectors cannot be followed across the crest due to sequence thinning and condensation. Borehole data from Cerritos-2, Norwalk-2, Pico-2 (Ponti et al., 2014; Bergen, 2015), and the Pico Rivera hole (inset) constrain the positions of time-correlative reflectors on either side of the fold crest. Structural relief across the forelimb and backlimb kink bands is estimated from the depth difference between crest and trough positions of each sequence top. The inset image shows the high-resolution seismic reflection profile, water monitoring well Pico 2, and the Pico Rivera borehole. Sequence boundaries identified in the Pico 2 well at the northern end of the section were correlated to discrete reflectors in the seismic profile and traced southward to the Pico Rivera borehole. The range of relief values calculated for the stratigraphic sequences reflects uncertainties in reflector–sequence boundary matching, seismic profile depth conversion, and the interpreted position of each sequence top within the Pico 2 borehole. A charcoal sample from a silt-rich horizon, interpreted as the top of the Mesa, provides additional age control for that contact. The high-resolution profile also provides some evidence for erosion of the upper Mesa on the upthrown side of the fold and/or markedly reduced sediment accumulation rates on that side.

Figure 5. Correlation of the top of the Gaspur aquifer across the crest of the Santa Fe Springs anticline as a function of elevation above sea level (ASL). The top of the Gaspur aquifer and the base of the Bellflower aquitard above it

is the contact between a coarse-grained sand or gravel and a fine-grained sand or silt unit above. This relatively shallow contact is well-constrained by a dense array of geotechnical holes throughout the city and boreholes from Leon et al. (2007) on Carfax Avenue (Figure 1b). The top of the Gaspur aquifer is folded at two distinct buried monoclinal scarps located at the upward projections of both the forelimb and the backlimb growth triangles. The drilling data allow us to measure the structural relief across the two growth triangles to provide a comparative measurement of forelimb and backlimb deformation during Holocene times.

3.5. Slip Rate Calculations

3.5.1. Uplift of Sequences

To quantify uplift during fold growth, we measured the absolute depth of each marker reflector's crest and trough relative to the ground surface, using a combination of the industry seismic reflection profile, the high-resolution seismic reflection profiles, and borehole data (Figure 4). These measurements provide a direct record of structural relief, which we interpret as the cumulative result of post-depositional folding and uplift within discrete kink bands on both the forelimb and the backlimb of the SFSA.

The sediments underlying the study area consist of laterally continuous, Pleistocene fluvial and minor marine deposits composed mainly of sands and gravel-bearing units. These sediments were originally deposited at low stream gradients (<1°) and because of their generally coarse grain size do not drape pre-existing topography but rather were deposited as near-horizontal units buttressing any pre-existing topography (e.g., fold scarps) (e.g., Blatt et al., 1980; Dolan et al., 2003; Leon et al., 2007). Drilling and seismic reflection data confirm that these strata maintain lateral continuity and exhibit no significant thickening on the downthrown sides of growth triangles, reinforcing the interpretation that deposition occurred at gentle stream gradients. We also accounted for uncertainties in the velocity structure of the Los Angeles Basin, which influence depth migration in seismic reflection data and must be considered as potential errors in extrapolating sequence tops from borehole data across the seismic reflection profiles.

This approach yielded a probability distribution of structural relief for each sequence top, allowing for a more robust quantification of deformation (Table 1, *Supplemental Table S4*). For a more detailed assessment of uncertainties in basin velocities and seismic depth conversions the reader is referred to Bergen et al. (2017).

Given this depositional framework, we interpret the measured structural relief as a direct manifestation of fold-related uplift within the kink bands. The exceptions are: (1) the top of the Gaspur aquifer, which occurs at an average depth of less than 15 m across the SFSA and is not readily discernible in any of the available seismic reflection data; and (2) the top of the Mesa on the forelimb of the SFSA. This horizon is also too shallow to be recognized in the industry seismic reflection profile and is difficult to discern in the high-resolution seismic reflection profile on the forelimb. Instead, the structural relief of the top of the Gaspur across the forelimb and backlimb kink bands, and the top of the Mesa on the forelimb kink band, was measured from the north-south transect of boreholes shown in Figure 5.

3.5.2. Calculating fault displacements

Having determined the geometry of both the fault ramp and the overlying folded strata, we apply fault-bend theory to calculate fault displacements since the deposition of each stratigraphic sequence (e.g., Suppe, 1983; Shaw et al., 2002; Connors et al., 2021; Don et al., 2022). The variables used to calculate fault displacements are **(1) the uplift** of the tops of the successive stratigraphic sequences (across the forelimb and backlimb growth triangles) measured using the seismic reflection and borehole data, and **(2) the dip of the three fault ramp segments** (Table 1, *Supplemental Materials*).

The displacement on the FLR since the deposition of a specific sequence is the structural relief of the top of that sequence across the forelimb kink band divided by the sine of the measured 27° dip of the thrust ramp beneath the forelimb (FLR) (Figure 3, Table 2). The structural relief in sequences folded across the backlimb kink band results from fault displacement through the fault-bend between the steepened (central) thrust ramp (BLR-S2) and the deeper, moderately dipping (lower) thrust ramp (BLR-S1). To calculate the BLR-S2 and BLR-S1 displacements we use trigonometric relationships determined by Don et al. (2022) between the dips of the backlimb fault segments and the backlimb uplift across the kink band (Figure 3, Table 2, *Supplemental Table S5*).

Table 2. Cumulative fault displacements of marker horizons

3.5.3. Middle Pleistocene to Holocene incremental slip rate record

We combined the ages of stratigraphic sequence tops with the calculated fault displacements to generate an incremental slip rate record for the FLR, BLR-S2, and BLR-S1 thrust segments at multiple periods during the past 1.4 million years (Table 3). Specifically, we used the ages of the stratigraphic sequence tops, which represent the youngest possible age for the preceding growth interval, to bracket each incremental displacement interval.

For each fault ramp segment, three incremental slip rate records were calculated using different basin velocity models (slow, fast, and preferred) for depth migration of the seismic reflection data (Section 6 of the *Supplemental Materials*). Variations in the adopted velocity structure produce systematic dip changes in the fault system (of approximately 2°) and corresponding differences in the amount of slip accommodated during fold growth. Only results from our preferred velocity model are discussed here, as they best fit previous observations (e.g., Shaw & Shearer, 1999; Allmendinger & Shaw, 2000; Bergen, 2015; Bergen et al., 2017) and match the stratigraphy documented in the borehole data. Accordingly, all tables report slip rates from this preferred model; results from alternative velocity models are provided in *Supplemental Table S5.*

Incremental slip rates were calculated using RISeR (https://github.com/rzinke/RISeR; Zinke et al., 2017, 2019), a Python-based software package that employs Markov Chain Monte Carlo

(MCMC) sampling to calculate slip rate probabilities between deformed marker horizons with known ages and accumulated slip. RISeR allows for the propagation of uncertainties inherent in all physical measurements (e.g., age uncertainties, uplift measurement uncertainties).

Uncertainties in slip rate calculations arise from (1) measurement errors of the absolute depth of troughs and crests of reflectors, (2) matching of continuous reflectors to sequence boundaries in boreholes, (3) the velocity model used for migration of the seismic reflection data, and (4) the ages of stratigraphic sequence tops. Despite these uncertainties, slip rate models using different seismic velocity parameters yield consistent patterns of relative fault displacements between the forelimb and backlimb ramp segments and consistent patterns of rate variation since middle Pleistocene time (*Supplemental Table S5* and *Supplemental Figure S8*).

Slip rate observations

Including the ground surface, we have eight dated marker horizons, defining seven intervals over which we calculate average slip rates on the thrust ramp beneath the backlimb and forelimb of the PHT. These intervals are from oldest to youngest: (1) the top of the upper Long Beach sequence to the top of the lower Wilmington sequence, which spans the interval from ~1400 to ~580 ka; (2) the top of the lower Wilmington sequence to the top of the upper Wilmington sequence (~580 to ~475 ka); (3) the top of the upper Wilmington sequence to the top of the Harbor sequence (~475 to ~160 ka); (4) the top of the Harbor sequence to the top of the Pacific sequence (~160 to ~110 ka); (5) the top of the Pacific sequence to the top of the Mesa sequence (~110 to ~21 ka); (6) the top of the Mesa sequence to the top of the Gaspur aquifer (~21 to ~10 ka); and (7) the top of the Gaspur sequence to the ground surface (~10 ka to present).

The incremental slip rate record we calculated for the PHT shows significant variation in rates over time, with incremental slip rates calculated for all ramp segments ranging from as slow as 0.2 mm/yr during the middle to late Pleistocene (~1400 to 160 ka), to as fast as 2.5 mm/yr during the latest Pleistocene and Holocene (past ~21.4 kyr) (Figure 6; Table 3). In general, the slip rate of the Santa Fe Springs segment of the PHT has increased during the past ca. 500,000 years. In particular we document a marked rate increase on both the forelimb and the backlimb at the time of deposition of the Harbor sequence sometime between ~200 and 117 ka.

To assess whether observed slip rate variations reflect genuine changes in fault behavior or rather result from data uncertainties, we compare probability distributions for successive time intervals. Although the MCMC sampling simulations (from RISeR) yield overlapping slip rate distribution tails, the overlap between post-Harbor and pre-Harbor slip rates is less than 5%. This limited overlap indicates that the observed four-fold increase in slip rate is unlikely to result from calculation errors and reflects a real change in fault behavior during late Pleistocene time.

Forelimb versus Backlimb fault displacements

In order to quantify slip partitioning along the fault ramp through time, we calculate the ratio of preferred forelimb to backlimb slip rates for each of the seven time intervals. We define this forelimb-to-backlimb slip rate ratio (FBSRR) as the slip rate on the forelimb ramp (FLR) divided by the slip rate on the steepened backlimb ramp (BLR-S2) for a given time interval. In the following, we simply refer to this ratio as the displacement ratio or the FBSRR.

The same backlimb uplift measurements and sequence ages were used to calculate the incremental slip rate record for the two backlimb thrust ramp segments BLR-S1 and BLR-S2 (Table 3). The displacement ratio (and thus the slip rate ratio) between these two segments is the “R-value,” a parameter derived from the geometric relationships of the backlimb ramp segments using the fault-bend folding formulation of Suppe (1983). Thus, because ramp segment BLR-S2 is steeper than ramp segment BLR-S1 forming a concave upward fault bend, BLR-S2 displacements and slip rates are consistently 12% greater than on BLR-S1 for all time intervals (Table 2).

To evaluate relative slip rates derived from the forelimb and backlimb through time, we compare the FBSRR over the seven intervals bounded by the successive sequence tops (Table 3). The reflector at the top of the upper Long Beach sequence records approximately 1.4 million years of cumulative displacement, with the FLR recording only 63% of the displacement observed on the BLR-S2. Our analyses reveal a low FBSRR of less than 0.51 between the deposition of the upper Long Beach and the lower Wilmington sequences (between ~1400 to ~580 ka). This ratio increases to an average of more than 0.8 between the upper Wilmington sequence and the Mesa sequence (between ~475 to 21 ka). The change from slip-ratio increase (increase in forelimb activity relative to the backlimb) to slip-ratio decrease (decrease in forelimb activity relative to the backlimb) occurred around the time of deposition of the Harbor sequence between ~200 and 117 ka. In the youngest part of the section, from the top of the Mesa sequence to the present (~21 ka to 0 ka), the FBSRR declines to an unexpectedly low value of less than 0.5. Although the FBSRR values do not incorporate formal uncertainty bounds, the magnitude of the observed temporal variability—particularly the large increases and decreases in slip-rate ratios—exceeds any plausible error range and would not affect the broader patterns of changes in slip partitioning between the FLR, BLR-S1, and BLR-S2 inferred by these ratios.

Table 3. Slip-Rates for the three fault segments

Figure 6. Incremental slip rate record for each of the three fault ramp segments. Preferred slip rates in mm/yr are shown as lines connecting points of preferred displacement and preferred sequence ages for ramp segments FLR (blue), BLR-S2 (red) and BLR-S1 (yellow). The rectangles show the range of the 1-sigma uncertainties for displacement and age of each sequence. The inset shows the slip rate recorded by the Harbor, Pacific, Mesa, and

Gaspur since 200 ka. Detailed slip rate results are shown in MCMC plots, for each fault ramp segment, in the Supplemental materials.

4. Discussion

The detailed incremental slip-rate record for the Santa Fe Springs segment of the Puente Hills blind-thrust fault (PHT), which we have documented, reveals a complex pattern of slip-rate variations since the deposition of the upper Long Beach sequence ca. 1.4 Ma. The data depict an evolving fault system with varied displacements across different fault ramp segments and a more than four-fold increase in slip-rate from late Pleistocene to Holocene time. These results have significant implications for understanding the kinematics and structural evolution of fault-related folds, for strain transfer between different fault segments and adjacent faults, and for seismic hazard analysis in the densely populated greater Los Angeles metropolitan region, which is home to more than 10 million people.

4.1. Forelimb versus Backlimb displacements and slip rate variability

The middle Pleistocene to present evolution of the Santa Fe Springs section of the PHT fold-fault system is elucidated by the ratio of forelimb-to-backlimb fault displacement over time. Direct comparisons of fault displacements beneath the forelimb and backlimb, recorded by uplifted seismic reflectors at the tops of regionally correlative stratigraphic sequences, show that displacements on the deep fault ramp segments (both BLR-S1 and BLR-S2) driving backlimb fold growth have experienced greater displacements than the shallower fault ramp segment (FLR) driving forelimb fold growth.

The data presented here do not allow for displacement comparisons prior to deposition of the upper Long Beach sequence before 1.4 Ma, but evidence of earlier backlimb growth through kink band migration is observed in Pliocene-Pleistocene strata of the upper part of the Fernando Formation, indicating fault-related folding has been active on the backlimb since at least 2.3 Ma (Shaw et al., 2002).

The displacement ratio (FBSRR) increased from as little as 0.36 (i.e., the forelimb records only 36 % of the displacement on the backlimb) before ca. 475 ka to approximately 0.7 between 160 ka and 475 ka, during deposition of the upper Wilmington and Harbor sequences. This indicates that backlimb growth was the primary mechanism for fault displacement until approximately 0.5 Ma, when forelimb growth began to accommodate significant strain. The ratio of forelimb to backlimb slip peaked at ~0.9 sometime between the deposition of the Harbor and Mesa sequences, between ~21 ka and 160 ka, declining thereafter to a ratio less than 0.5.

The increase in forelimb displacement relative to backlimb displacement after ~475 ka marks the initiation of fault-bend folding accommodating slip on the forelimb, with material displaced onto a horizontal or subhorizontal detachment at the tip of the PHT that extends south into the central Los Angeles Basin (Shaw et al., 2002). Supporting evidence for the establishment of the forelimb fault-bend folding of the PHT during this period comes from industry seismic reflection data, which show parallel synclinal and anticlinal axial surfaces beneath the reflector at the top of the upper Wilmington sequence—indicating that these pre-growth strata were deposited before the formation of the forelimb kink band (Figure 4). The late Pleistocene forelimb to backlimb slip ratio of 0.9 is consistent with the prediction for a well-established fault-bend fold (Suppe, 1983; Shaw et al., 2005).

For the two youngest intervals that we analyzed, spanning the last ~21 ky, however, the displacement ratio (FBSRR) is much lower (0.40 to 0.46) than the 0.9 ratio observed during the previous > 100 ky after establishment of the forelimb fault-bend fold. Such a marked decrease in the FBSRR in the youngest intervals we study is a surprising observation in a well-developed fault-bend fold system like the SFSA. This ratio could reflect either an anomalously slow forelimb slip rate relative to the backlimb, or an anomalously fast backlimb slip rate relative to the forelimb.

There are several possible explanations for these young, anomalously low ratios, including: (1) erosion of either the forelimb hangingwall block or erosion of the backlimb footwall block; (2) recent changes in the kinematics of the fault-bend fold system, such as a decrease in forelimb slip due to increased resistance to fault slip on the fault flat above the top of the ramp (e.g., Hughes et al., 2014); and/or (3) recent acceleration of slip on a backthrust observed in industry wells within the backlimb of the SFSA at a depth of ~1 km (pink line in Figure 2); slip on this backthrust would contribute to structural relief of the backlimb, while reducing the amount of slip.

Although erosion of the upthrown side of the forelimb kink band or erosion of the downthrown side of the backlimb kink band would generate an anomalously low FBSRR, evidence for significant erosion is poorly constrained by available borehole and seismic reflection data within the youngest stratigraphic interval that records deposition over the past ~21 ka. Moreover, we consider it unlikely that the kinematics of this well-established fault-bend fold system would have changed fundamentally over such a short time interval. Finally, the backthrust observed in industry wells exhibits only minor offset, making it improbable that slip on this structure has been sufficient to drive the observed shift in displacement ratios in the shallow subsurface. Taken together, these considerations indicate that, while several plausible mechanisms exist, the available stratigraphic, geomorphic, and subsurface data are presently insufficient to discriminate among them or to uniquely resolve the cause of the Holocene decrease in FBSRR.

Regardless of the mechanism responsible for this decrease in FBSRR, these data demonstrate that fault activity after deposition of the Long Beach sequence but prior to deposition of the Harbor sequence (between ~475 ka and 580 ka) was relatively slow, with thrust slip rates between ~0.2 mm/yr and ~0.8 mm/yr. A significant increase in slip rate occurred around the time of deposition of the top of the Harbor sequence (between ~117 ka and 200 ka), accelerating from ~0.3 mm/yr to ~1.2 mm/yr on the forelimb and from ~0.4 mm/yr to ~1.3 mm/yr on the backlimb. Bergen et al. (2017) observed a similar increase in fault slip rate at approximately the same time on the western, Los Angeles segment of the PHT, with slip rates accelerating from ~0.45 mm/yr in the late Pleistocene (between ca. 288 ka and ca. 163.5 ka) to ~1.33 mm/yr in the Holocene (ca. 15 ka to present day). This indicates coordinated behavior of both the Los Angeles and Santa Fe Springs segments of the PHT and suggests that there was a significant change in the kinematics of the contractional fault system beneath the northern Los Angeles metropolitan region ca. 160 ka. As noted above, this distinct increase in slip rate is temporally correlated with the peak in the FBSRR, which we interpret as recording the initiation of full forelimb folding and the establishment of the fault-bend fold kinematics that have defined the structure since ca. 160 ka, despite evidence for at least some activity on the forelimb prior to this time. Our record gives no indication of the slip rate slowing up to the present, and indeed rates calculated from the backlimb folding show a continued increase in slip rate into the Holocene, with slip rates averaged from ca. 160 ka to present of ~1.7 mm/yr relative to the Holocene slip rate averaged since ca. 10 ka of ~2.4 mm/yr. This would suggest that the slip rate of the Santa Fe Springs segment of the PHT measured on the basis of backlimb folding above the deep thrust ramp has accelerated in the latest Pleistocene and Holocene time.

4.2. Comparison with other contractional faults in the Los Angeles Basin accommodating North-South shortening

A striking discrepancy exists in the Los Angeles Basin between fault slip-deficit rates calculated on the basis of modelling of geodetic data relative to longer-term geologic fault slip rates. Specifically, geodetic data indicate that north-south shortening of the Los Angeles metropolitan region is occurring at a rate of ~8 - 9 mm/yr (Rollins et al., 2018). Modeling of these geodetic data suggests that most of this strain accumulation is associated with several major reverse faults, including the Puente Hills blind-thrust fault, the Sierra Madre fault, and the Compton blind thrust fault. The models suggests slip-deficit rates of 3 - 4 mm/yr on these thrust faults, yet previous geologic measurements of the latest Pleistocene-Holocene slip rates on most of these faults reveal much slower longer-term average geologic slip rates on the order of < 1 to ~1.5 mm/yr (e.g., Crook et al., 1987; Tucker & Dolan, 2001; Shaw et al., 2002; Dolan et al., 2003; Myers et al., 2003; Leon et al., 2007; 2009; Bergen et al., 2017; Burgette et al., 2020). At 2.4 ± 0.26 mm/yr, however, the best-estimate Holocene slip rate we generate from the backlimb folding above the deep ramp of the PHT SFS is much faster than the long-term (~1.6 Ma to present) average slip rate of 0.44 - 0.82 mm/yr determined by Shaw et al. (2002) and the Holocene slip rate derived from the forelimb folding of ≥ 0.9 to 1.6 mm/yr, as was originally suggested by Dolan et al. (2003) and Leon et al. (2007).

The geodetic–geologic rate discrepancy is particularly pronounced if we were to use the Holocene PHT slip rate derived from the forelimb folding of ~1.1 ± 0.1 mm/yr, as originally suggested by Dolan et al. (2003) and Leon et al. (2007). As detailed above, however, the PHT forelimb slip rate is a minimum rate relative to the slip rate of the deeper ramp both because some shortening is consumed by folding between the forelimb and backlimb growth triangles of the SFSA, and because the decrease in the ratio of forelimb to backlimb folding indicates that a significant portion of the slip on the deep thrust ramp has not extended updip along the thrust ramp and all the way through the fault tipline during Holocene time. In contrast, although the revised, much faster best-estimate Holocene slip rate for the PHT of ~2.4 mm/yr that we document partially closes the gap between the geodetically defined slip-deficit rate for the Santa Fe Springs segment of the PHT, overall the geodetic data suggest that strain is accumulating on the urban fault network beneath the Los Angeles metropolitan region at much faster rates than would be suggested on the basis of the cumulative geologic fault slip rates on these structures. This, despite the fact that the entire ~250-year-long historic period, and likely the past ≥ 1,000 years, has been a period of anomalously low seismic energy release (Dolan et al., 1995, 2007), with much more elastic strain energy accumulating on the urban faults than has been released during this period. However, it should be noted that some of this rate discrepancy might be reduced if uncertainties in the geodetic modelling framework are considered, including underestimation of the influence of strike-slip faults, the role of bulk crustal compaction, and incomplete representation of shortening accommodated by smaller or poorly characterized structures in the Los Angeles Basin; future modelling studies of the geodetic surface deformation field could potentially reduce the magnitude of this discrepancy.

These results suggest that either the rate of elastic strain accumulation has recently accelerated on the urban fault network beneath Los Angeles, or that we have insufficient resolution on latest Pleistocene-Holocene slip rates for many of these urban faults to discern any potential late Holocene acceleration in seismic fault slip that might explain the current rapid rates of elastic strain accumulation observed with geodetic data.

4.3. Seismic hazard implications

The increase in fault slip rate since late Pleistocene time observed on both the Los Angeles segment and the Santa Fe Springs segment of the PHT suggests either an increase in earthquake frequency or an increase in displacement per earthquake, as noted by Bergen et al. (2017) for the western Los Angeles segment of the PHT.

Paleoseismic studies of the PHT reveal the presence of well-defined paleo-fold scarps, that are interpreted as recording co-seismic fold growth (Dolan et al., 2003; Leon et al., 2007). Such coseismic fold-growth has been observed in large-magnitude earthquakes (e.g., 1980 El Asnam, 1983 Coalinga, and 1999 Chi-Chi), whereas there is no compelling geologic or geodetic evidence that fault-related folds grow predominantly via aseismic or interseismic creep mechanisms (Yielding et al., 1981; Stein & King, 1984; Chen et al., 2007).

Although paleoseismic evidence shows that the PHT has generated multiple $M_w > 7$ earthquakes during Holocene time (Dolan et al., 2003; Leon et al., 2007), the 1987 $M_L = 5.9$ Whittier Narrows earthquake (Hauksson & Jones, 1989) is the largest earthquake generated by the PHT since the establishment of Los

Angeles in the late 1700s. Despite its moderate size, the 1987 earthquake caused more than $200 million in damage and demonstrated that even relatively small earthquakes generated by the PHT pose a significant seismic threat to metropolitan Los Angeles (Field et al., 2005). Indeed, because of the location of the PHT directly beneath the heart of the metropolitan Los Angeles region, coupled with the fault's north-dipping geometry, which will focus seismic waves directly into the core of the urban city center and the Los Angeles Basin, and its slip rate documented here, the PHT represents one of the greatest seismic risks in the United States (e.g., Dolan et al., 2003; Leon et al., 2007; Field et al., 2005), and any increase in either the frequency or the magnitude of major PHT earthquakes that is used in the development of probabilistic seismic hazard assessment (e.g., the Uniform California Earthquake Rupture Forecast version 3 model; Field et al., 2015) is a key concern for this region.

Our observations show that, on average since the inception of the current fault-bend fold kinematics of the Santa Fe Springs segment of the PHT ca. 170 ka, approximately 80% of fault displacement recorded by backlimb folding is accommodated on the forelimb. This indicates that at least since the late Pleistocene the forelimb growth triangle records ≤ 80 % of the total slip at depth on the deep thrust ramp. Consequently, seismic hazard assessments based solely on forelimb data will significantly underestimate the full slip rate of the fault, with a commensurate underestimation of the probabilistic seismic hazard posed by the fault.

The marked increase in slip rate since ~21 ka may partially reconcile the long-standing discrepancy between geologic and geodetic slip-rate estimates, a discrepancy that directly impacts seismic hazard assessments for metropolitan Los Angeles. Long-term geologic slip rates from the forelimb (~0.6 mm/yr) and Holocene rates for the forelimb calculated here (~1.1 mm/yr) are substantially lower than the 3 – 4 mm/yr strain accumulation rates modeled by Rollins et al. (2018), but are more closely aligned with

Holocene age backlimb slip rates (> 2.4 mm/yr) for the SFSA. However, even when backlimb data are included, a significant gap remains between geologic and geodetic estimates.

If true, this discrepancy could indicate a higher probability of near-future earthquake recurrence relative to the long-term average geological fault slip rates in current seismic hazard assessments, or the discrepancy may reflect unmodeled off-fault deformation or limitations in the rheological and structural assumptions underlying current geodetic inversions. Alternatively, this discrepancy could reflect the lack of detailed incremental slip-rate records for latest Pleistocene-Holocene time for all of the major faults of the Los Angeles metropolitan region. Resolving this issue will require higher temporal resolution incremental slip rate data than are currently available, as well as improved models of basin geometry, basement depth, and elastic properties used in forward and inverse modeling. This discrepancy remains a fundamental uncertainty with significant implications for evaluating the seismic potential of the blind thrust systems beneath metropolitan Southern California.

5. Conclusions

Our long-term record of incremental fold growth elucidates the progressive development of the Santa Fe Springs segment of the Puente Hills blind-thrust fault (PHT) at seven different time steps, providing a more detailed understanding of the structural evolution of the system, the role played by the PHT in the active tectonics of southern California, and the seismic threat the PHT poses to the greater Los Angeles metropolitan region. Our analysis indicates that from ca. 1.4 Ma to ca. 475 ka, the forelimb folding exhibits only 36 to 52 % of the deep thrust displacement recorded on the backlimb, indicating that the majority of slip during this phase was accommodated by backlimb growth. Subsequent to ~475 ka, the forelimb rate increases, with the forelimb recording as much as 92% of the displacement measured on the backlimb, suggesting an increased role of forelimb folding in accommodating deep thrust displacement and stabilization of fold growth dynamics that persists to the present day. In addition to the basic change in the dynamics of the system ca. 475 ka, we document a pronounced increase in slip rate sometime between ~475 and 160 ka, with thrust slip rates based on forelimb folding accelerating from ~0.3 mm/yr to ~1.2 mm/yr, relative to backlimb thrust slip rates that accelerate from ~0.4 mm/yr to ~2.4 mm/yr (Holocene maximum). A similar acceleration in thrust slip rate at approximately the same time was observed on the western Los Angeles segment of the PHT by Bergen at al. (2017) indicates that the two fault segments are behaving in concert.

Consistently faster displacement rates on the backlimb compared to the forelimb suggest that slip rates derived from forelimb growth strata likely underestimate the slip rate of the deeper seismogenic portions of blind thrust faults like the PHT. In the case of the PHT, this discrepancy may partially explain differences between slower geological fault slip rates and geodetic slip-deficit rates of elastic strain accumulation. Inasmuch as some early estimates of the current slip rate of the PHT were based on analyses of forelimb folding (e.g., Dolan et al., 2003; Leon et al., 2007), the seismic hazard posed by the PHT may be greater than initially estimated. Using the thrust displacement rates we derived from backlimb folding, the PHT exhibits a latest Pleistocene-Holocene average thrust slip rate of ~1.4 mm/yr (since the deposition of the Pacific ca. 110 ka), consistent with the rate of occurrence of large-magnitude ($M_w \geq 7$) paleo-earthquakes observed across the forelimb of the fault by Dolan et al. (2003) and Leon et al. (2007). These results highlight the seismic threat posed by the PHT. Specifically, the location of the PHT directly beneath the core of the Los Angeles metropolitan region, home to more than 10 million people, coupled with its north-dipping geometry, will focus seismic wave energy up-dip beneath downtown Los Angeles and into the deep Los Angeles Basin, underscoring the potential for severe ground shaking. Evidence for kinematic linkage between at least the western and central segments of the PHT, together with the relatively fast latest Pleistocene–Holocene average slip rate documented here, further indicates that the PHT represents one of the largest deterministic seismic hazards in the United States.

6. Acknowledgements

We thank the many people who assisted in the acquisition of all of the different data sets used in this analysis, including students from the University of Southern California, Harvard University, and the Statewide California Earthquake Center (SCEC) summer Intern program, as well as USGS personnel and personnel from the University of Nevada-Las Vegas and New Mexico Tech, who provided the vibrator and associated expertise. We also thank the cities of Los Angeles, Bellflower, Fullerton, and Pico Rivera for permission to conduct our research on city property. We gratefully acknowledge funding support for the many projects incorporated into this study provided by multiple grants from the U.S. National Science Foundation, the U.S. Geological Survey, the Statewide California Earthquake Center, the University of Southern California Department of Earth Sciences, and Harvard University. We also thank reviewers Chris Rollins, Alexandra Hatem, and an anonymous reviewer for their helpful and constructive comments on this manuscript.

7. Open Research

The displacement and age model datasets, as well as the drilling database supporting the findings of this study are publicly available at Anthonissen (2025). Slip rate probability distributions were generated using the RISeR software package described in Zinke et al. (2019), which applies a Bayesian MCMC approach to estimate rates of slip accumulation between dated marker horizons.

The raw data and software supporting this study are available in FAIR-compliant repositories and are cited in the reference list below.

The seismic reflection profiles are archived in a U.S. Geological Survey data release available at Pratt (2026; https://doi.org/10.5066/P1XIR92T).

8. References

Aitken, M. J. (1998). Introduction to Optical Dating: The Dating of Quaternary Sediments by the Use of Photon-stimulated Luminescence. Clarendon Press: Oxford, UK, 280 pp. https://doi.org/10.1093/oso/9780198540922.001.0001

Aitken, M. J., & Xie, J. (1990). Moisture correction for annual gamma dose. Ancient TL, 8(2), 6-9. https://doi.org/10.26034/la.atl.1990.157

Allmendinger, R. W., & Shaw, J. H. (2000). Estimation of fault propagation distance from fold shape: Implications for earthquake hazard assessment. Geology, 28(12), 1099-1102. https://doi.org/10.1130/0091-7613(2000)28<1099:EOFPDF>2.0.CO;2

Anthonissen, C. (2025). Uplift Measurements, Displacement Calculations, Drilling Database, and RISeR outputs for the Santa Fe Springs Segment of the Puente Hills Thrust Fault [Data set]. Zenodo. https://doi.org/10.5281/zenodo.16047504

Argus, D. F., Heflin, M. B., Peltzer, G., Crampé, F., & Webb, F. H. (2005). Interseismic strain accumulation and anthropogenic motion in metropolitan Los Angeles. Journal of Geophysical Research: Solid Earth, 110(B4), B04401. https://doi.org/10.1029/2003JB002934

Balescu, S., & Lamothe, M. (1994). Comparison of TL and IRSL age estimates of feldspar coarse grains from waterlain sediments. Quaternary Science Reviews, 13(5-7), 437-444. https://doi.org/10.1016/0277-3791(94)90056-6

Bassinot, F. C., Labeyrie, L. D., Vincent, E., Quidelleur, X., Shackleton, N. J., & Lancelot, Y. (1994). The astronomical theory of climate and the age of the Brunhes-Matuyama magnetic reversal. Earth and Planetary Science Letters, 126(1-3), 91-108. https://doi.org/10.1016/0012-821X(94)90244-5

Benesh, N. P., Plesch, A., Shaw, J. H., & Frost, E. K. (2007). Investigation of growth fault bend folding using discrete element modeling: Implications for signatures of active folding above blind thrust faults. Journal of Geophysical Research: Solid Earth, 112(B3), B03S04. https://doi.org/10.1029/2006JB004466

Bergen, K. J. (2015). Pleistocene to modern deformation of the central Los Angeles basin. Doctoral dissertation, Harvard University: Cambridge, MA, 159 pp.

Bergen, K. J., Shaw, J. H., Leon, L. A., Dolan, J. F., Pratt, T. L., Ponti, D. J., Morrow, E., Barrera, W., Rhodes, E.J., Murari, M.K., & Owen, L. A. (2017). Accelerating slip rates on the Puente Hills blind thrust fault system beneath metropolitan Los Angeles, California, USA. Geology, 45(3), 227-230. https://doi.org/10.1130/G38520.1

Blake, G. H. (1991). Review of the Neogene Biostratigraphy and Stratigraphy of the Los Angeles Basin and Implications for Basin Evolution. In: Biddle, K. T. (ed.) Active Margin Basins: AAPG Memoir 52. American Association of Petroleum Geologists: Tulsa, OK, pp. 135-184. https://doi.org/10.1306/M52531C4

Blatt, H., Middleton, G. V., & Murray, R. C. (1980). Origin of Sedimentary Rocks, 2nd Edition, Prentice-Hall: Englewood Cliffs, NJ, 782 pp.

Burgette, R. J., Hanson, A. M., Scharer, K. M., Rittenour, T. M., & McPhillips, D. (2020). Late Quaternary slip rate of the Central Sierra Madre fault, southern California: Implications for slip partitioning and earthquake hazard. Earth and Planetary Science Letters, 530, 115907. https://doi.org/10.1016/j.epsl.2019.115907

Buylaert, J. P., Murray, A. S., Thomsen, K. J., Jain, M. (2009). Testing the potential of an elevated temperature IRSL signal from K-feldspar. Radiation Measurements, 44(5-6), 560-565. https://doi.org/10.1016/j.radmeas.2009.02.007

California Department of Water Resources (CDWR) (1961). Planned utilization of the ground water basins of the coastal plain of Los Angeles County, Appendix A: Ground Water Geology. California Department of Water Resources Southern District Bulletin 104, 191 pp., Available at https://archive.org/details/appdxplannedutilizati104calirich/page/n7/mode/2up (accessed DATE).

Chen, Y. G., Lai, K. Y., Lee, Y. H., Suppe, J., Chen, W. S., Lin, Y. N. N., Wang, Y., Hung, J.H., & Kuo, Y. T. (2007). Coseismic fold scarps and their kinematic behavior in the 1999 Chi-Chi earthquake Taiwan. Journal of Geophysical Research: Solid Earth, 112(B3), B03S02. https://doi.org/10.1029/2006JB004388

Connors, C. D., Hughes, A. N., & Ball, S. M. (2021). Forward kinematic modeling of fault-bend folding. Journal of Structural Geology, 143, 104252. https://doi.org/10.1016/j.jsg.2020.104252

Crook, R., Allen, C. R., Kamb, B., Payne, C. M., & Proctor, R. J. (1987). Quaternary geology and seismic hazard of the Sierra Madre and associated faults, western San Gabriel Mountains. In: Morton, D., & Yerkes,

R. F. (eds.) Recent Reverse Faulting in the Transverse Ranges, California. U.S. Geological Survey Profesional Paper 1339, pp. 7-26. https://doi.org/10.3133/pp1339

Davis, T. L., Namson, J., & Yerkes, R. F. (1989). A cross section of the Los Angeles area: Seismically active fold and thrust belt, the 1987 Whittier Narrows earthquake, and earthquake hazard. Journal of Geophysical Research: Solid Earth, 94(B7), 9644-9664. https://doi.org/10.1029/JB094iB07p09644

Dolan, J. F., Sieh, K., Rockwell, T. K., Yeats, R. S., Shaw, J., Suppe, J., Huftile, G.J., & Gath, E. M. (1995). Prospects for larger or more frequent earthquakes in the Los Angeles metropolitan region. Science, 267(5195), 199-205. https://doi.org/10.1126/science.267.5195.199

Dolan, J. F., Christofferson, S. A., & Shaw, J. H. (2003). Recognition of paleoearthquakes on the Puente Hills blind thrust fault, California. Science, 300(5616), 115-118. https://doi.org/10.1126/science.1080593

Dolan, J. F., Bowman, D. D., & Sammis, C. G. (2007). Long-range and long-term fault interactions in Southern California. Geology, 35(9), 855-858. https://doi.org/10.1130/G23789A.1

Don, J., Shaw, J. H., Nicolae, A. L., Sorlien, C. C., Nicholson, C., & Plesch, A. (2022). Late Pleistocene Slip Rate and 3D Geometry of the Mid-Channel Blind Thrust, Santa Barbara Channel, California, and Their Implications for Earthquake Hazards. Bulletin of the Seismological Society of America, 112(6), 3081-3101. https://doi.org/10.1785/0120220048

Durcan, J., King, G. E., Duller, G. A. T. (2015). DRAC: Dose Rate and Age Calculator for trapped charge dating. Quaternary Geochronology 28, 54-61. https://doi.org/10.1016/j.quageo.2015.03.012

Edwards, B. D., Ehman, K. D., Ponti, D. J., Reichard, E. G., Tinsley, J. C., Rosenbauer, R. J., & Land, M. (2009). Stratigraphic controls on saltwater intrusion in the Dominguez Gap area of coastal Los Angeles. In: Lee, H. J., & Normack, W. R. (eds.) Earth Science in the Urban Ocean: The Southern California Continental Borderland. Geological Society of America Special Paper 454: Boulder, CO, pp. 375-395. https://doi.org/10.1130/2009.2454(5.4)

Ehman, E. D., & Edwards, B. D. (2017). Defining aquifer architecture using seismic and sequence stratigraphy in the Los Angeles basin, California: A foundation for future assessment and management of groundwater resources. 2017 American Association of Petroleum Geologists Annual Convention & Exposition, April 2-5, Houston, TX, 18 pp.

Field, E. H., Seligson, H. A., Gupta, N., Gupta, V., Jordan, T. H., & Campbell, K. W. (2005). Loss estimates for a Puente Hills blind-thrust earthquake in Los Angeles, California. Earthquake Spectra, 21(2), 329-338. https://doi.org/10.1193/1.1898332

Field, E. H., Biasi, G. P., Bird, P., Dawson, T. E., Felzer, K. R., Jackson, D. D., Johnson, K.M., Jordan, T.H., Madden, C., Michael, A. J., Milner, K. R., Page, M. T., Parsons, T., Powers, P. M., Shaw, B. E., Thatcher, W.

R., Weldon, R. J., & Zeng, Y. (2015). Long-term time-dependent probabilities for the third Uniform California Earthquake Rupture Forecast (UCERF3). Bulletin of the Seismological Society of America, 105(2A), 511-543. https://doi.org/10.1785/0120140093

Gauriau, J., & Dolan, J. F. (2021). Relative structural complexity of plate-boundary fault systems controls incremental slip-rate behavior of major strike-slip faults. Geochemistry, Geophysics, Geosystems, 22(11), e2021GC009938. https://doi.org/10.1029/2021GC009938

Gauriau, J., & Dolan, J. (2024). Comparison of geodetic slip-deficit and geologic fault slip rates reveals that variability of elastic strain accumulation and release rates on strike-slip faults is controlled by the relative structural complexity of plate-boundary fault systems. Seismica, 3(1), 1119. https://doi.org/10.26443/seismica.v3i1.1119

Guérin, G., Mercier, N., Adamiec, G. (2011). Dose-rate conversion factors: Update. Ancient TL, 29(1), 5-8. https://doi.org/10.26034/la.atl.2011.443

Guzofski, C. A., Shaw, J. H., Lin, G., & Shearer, P. M. (2007). Seismically active wedge structure beneath the Coalinga anticline, San Joaquin basin, California. Journal of Geophysical Research: Solid Earth, 112(B3), B03S05. https://doi.org/10.1029/2006JB004465

Hauksson, E., & Jones, L. M. (1989). The 1987 Whittier Narrows earthquake sequence in Los Angeles, southern California: Seismological and tectonic analysis. Journal of Geophysical Research: Solid Earth, 94(B7), 9569-9589. https://doi.org/10.1029/JB094iB07p09569

Hauksson, E. (1990). Earthquakes, faulting, and stress in the Los Angeles basin. Journal of Geophysical Research: Solid Earth, 95(B10), 15365-15394. https://doi.org/10.1029/JB095iB10p15365

Hughes, A. N., Benesh, N. P., & Shaw, J. H. (2014). Factors that control the development of fault-bend versus fault-propagation folds: Insights from mechanical models based on the discrete element method (DEM). Journal of Structural Geology, 68(A), 121-141. https://doi.org/10.1016/j.jsg.2014.09.009

Huntley, D. J., & Baril, M. R. (1997). The K content of the K-feldspars being measured in optical dating or in the thermoluminescence dating. Ancient TL, 15(1), 11-13. https://doi.org/10.26034/la.atl.1997.271

Huntley, D. J., & Hancock, R. G. V. (2001). The Rb contents of the K-feldspar grains being measured in optical dating. Ancient TL, 19(2), 43-46. https://doi.org/10.26034/la.atl.2001.333

Huntley, D. J., & Lamothe, M. (2001). Ubiquity of anomalous fading in K-feldspars and the measurement and correction for it in optical dating. Canadian Journal of Earth Sciences, 38(7), 1093-1106. https://doi.org/10.1139/e01-013

Keller, E. A., Zepeda, R. L., Rockwell, T. K., Ku, T. L., & Dinklage, W. S. (1998). Active tectonics at Wheeler ridge, southern San Joaquin valley, California. Geological Society of America Bulletin, 110(3), 298-310. https://doi.org/10.1130/0016-7606(1998)110<0298:ATAWRS>2.3.CO;2

Lamothe, M., Auclair, M., Hamzaoui, C., & Huot, S. (2003). Towards a prediction of long-term anomalous fading of feldspar IRSL. Radiation Measurements, 37(4-5), 493-498. https://doi.org/10.1016/S1350-4487(03)00016-7

Land, M., Everett, R. R., & Crawford, S. M. (2002). Geologic, hydrologic, and water-quality data from multiple-well monitoring sites in the Central and West Coast Basins, Los Angeles County, California, 1995-2000. U.S. Geological Survey Open-File Report 2001-277, 178 pp. https://doi.org/10.3133/ofr01277

Land, M., Reichard, E. G., Crawford, S. M., Everett, R. R., Newhouse, M. W., & Williams, C. F. (2004). Ground-water quality of coastal aquifer systems in the West Coast Basin, Los Angeles County, California, 1999–2002. U.S. Geological Survey Scientific Investigations Report 2004-5067, 88 pp. https://doi.org/10.3133/sir20045067

Lawson, M. J., Roder, B. J., Stang, D. M., & Rhodes, E. J. (2012). OSL and IRSL characteristics of quartz and feldspar from southern California, USA. Radiation Measurements, 47(9), 830-836. https://doi.org/10.1016/j.radmeas.2012.03.025

Leon, L. A., Christofferson, S. A., Dolan, J. F., Shaw, J. H., & Pratt, T. L. (2007). Earthquake-by-earthquake fold growth above the Puente Hills blind thrust fault, Los Angeles, California: Implications for fold kinematics and seismic hazard. Journal of Geophysical Research: Solid Earth, 112(B3), B03S03. https://doi.org/10.1029/2006JB004461

Leon, L. A., Dolan, J. F., Shaw, J. H., & Pratt, T. L. (2009). Evidence for large Holocene earthquakes on the Compton thrust fault, Los Angeles, California. Journal of Geophysical Research: Solid Earth, 114(B12), B12305. https://doi.org/10.1029/2008JB006129

Leon, L. A. (2009). Paleoseismology of blind-thrust faults beneath Los Angeles, California: Implications for the potential of system-wide earthquakes to occur in an active fold-and-thrust belt. Doctoral dissertation, University of Southern California: Los Angeles, CA, 266 pp. https://doi.org/10.25549/usctheses-m2497

McAuliffe, L. J., Dolan, J. F., Rhodes, E. J., Hubbard, J., Shaw, J. H., & Pratt, T. L. (2015). Paleoseismologic evidence for large-magnitude (Mw 7.5–8.0) earthquakes on the Ventura blind thrust fault: Implications for multifault ruptures in the Transverse Ranges of southern California. Geosphere, 11(5), 1629-1650. https://doi.org/10.1130/GES01123.1

McDougall, K., Hillhouse, J., Powell, C. L., Mahan, S., Wan, E., & Sarna-Wojcicki, A. M. (2012). Paleontology and geochronology of the Long Beach core sites and monitoring wells, Long Beach, California: U.S. Geological Survey Open-File Report 2011-1274, 235 pp., 18 plates. https://doi.org/10.3133/ofr20111274

Medwedeff, D. A. (1992). Geometry and kinematics of an active, laterally propagating wedge-thrust, Wheeler Ridge, California. In: Mitra, S., & Fisher, G. W. (eds.) Structural Geology of Fold and Thrust Belts. Johns Hopkins University Press: Baltimore, MD, pp. 3-28.

Mejdahl, V. (1979). Thermoluminescence dating: Beta-dose attenuation in quartz grains. Archaeometry, 21(1), 61-72. https://doi.org/10.1111/j.1475-4754.1979.tb00241.x

Mueller, K., & Suppe, J. (1997). Growth of Wheeler Ridge anticline, California: Geomorphic evidence for fault-bend folding behaviour during earthquakes. Journal of Structural Geology, 19(3-4), 383-396. https://doi.org/10.1016/S0191-8141(96)00112-5

Murray, A. S., Wintle, A. G. (2000). Luminescence dating of quartz using an improved single aliquot regenerative-dose protocol. Radiation Measurements, 32(1), 57-73. https://doi.org/10.1016/S1350-4487(99)00253-X

Murray, A. S., Wintle, A. G. (2003). The single aliquot regenerative dose protocol: Potential for improvements in reliability. Radiation Measurements, 37(4-5), 377-381. https://doi.org/10.1016/S1350-4487(03)00053-2

Myers, D. J., Nabelek, J. L., & Yeats, R. S. (2003). Dislocation modeling of blind thrusts in the eastern Los Angeles basin, California. Journal of Geophysical Research: Solid Earth, 108(B9), 2443. https://doi.org/10.1029/2002jb002150

Novoa, E., Suppe, J., & Shaw, J. H. (2000). Inclined-shear restoration of growth folds. AAPG Bulletin, 84(6), 787-804. https://doi.org/10.1306/A96733F6-1738-11D7-8645000102C1865D

Oskin, M., Sieh, K., Rockwell, T., Miller, G., Guptill, P., Curtis, McArdle, M., & Elliot, P. (2000). Active parasitic folds on the Elysian Park anticline: Implications for seismic hazard in central Los Angeles, California. Geological Society of America Bulletin, 112(5), 693-707. https://doi.org/10.1130/0016-7606(2000)112<693:APFOTE>2.0.CO;2

Paulinski, S., Faunt, C., Land, M., Nishikawa, T., & Martin, P. (2023). Development of a Groundwater-Simulation Model in the Los Angeles Coastal Plain, Los Angeles County, California. U.S. Geological Survey Scientific Investigations Report 2021-5088, 489 pp. https://doi.org/10.3133/sir20215088

Plesch, A., Shaw, J. H., Benson, C., Bryant, W.A., Carena, S., Cooke, M., Dolan, J., Fuis, G., Gath, E., Grant, L., Hauksson, E., Jordan, T. H., Kamerling, M. J., Legg, M. R., Lindvall, S. C., Magistrale, H., Nicholson, C., Niemi, N. A., Oskin, M. E., Perry, S. C., Planansky, G., Rockwell, T. K., Shearer, P. M., Sorlien, C. C., Suess, M. P., Suppe, J., Treiman, J. A., & Yeats, R. S. (2007). Community fault model (CFM) for southern California. Bulletin of the Seismological Society of America, 97(6), 1793-1802. https://doi.org/10.1785/0120050211

Poland, J. F., Piper, A. M., & others (1956). Ground-water geology of the coastal zone, Long Beach-Santa Ana area, California. U.S. Geological Survey Water-Supply Paper 1109, 162 pp. https://doi.org/10.3133/wsp1109

Poland, J. F., Garrett, A. A., & Sinnott, A. (1959). Geology, hydrology, and chemical character of ground waters in the Torrance-Santa Monica area, California. U.S. Geological Survey Water-Supply Paper 1461, 425 pp. https://doi.org/10.3133/wsp1461

Ponti, D. J. (1989). Aminostratigraphy and chronostratigraphy of Pleistocene marine sediments, southwestern Los Angeles basin, California. Doctoral dissertation, University of Colorado at Boulder: Boulder, CO, 484 pp.

Ponti, B. D. J., Ehman, K. D., Edwards, B. D., Tinsley, J. C., Hildenbrand, T., Hillhouse, Hanson, R.T., McDougall, K., Powell C.L., Wan E., Land, M., Mahan, S., & Sarna-Wojcicki, A.M. (2007). Replenishment

District of Southern California A 3-dimensional model of water-bearing sequences in the Dominguez Gap region, Long Beach, California. U.S. Geological Survey Open-File Report 2007-1013, 34 pp. https://doi.org/10.3133/ofr20071013

Ponti, D. J., Wagner, B. J., Land, M., & Landon, M. K. (2014). Characterization of potential transport pathways and implications for groundwater management near an anticline in the Central Basin area, Los Angeles County, California. U.S. Geological Survey Open-File Report 2014-1087, 124 pp., 1 plate. https://doi.org/10.3133/ofr20141087

Powell II, C. L., & Stevens, D. (2000). Age and paleoenvironmental significance of mega-invertebrates from the" San Pedro" Formation in the Coyote Hills, Fullerton and Buena Park, Orange County, southern California. U.S. Geological Survey Open-File Report 2000-319, 83 pp. https://doi.org/10.3133/ofr2000319

Pratt, T. L., Shaw, J. H., Dolan, J. F., Christofferson, S. A., Williams, R. A., Odum, J. K., & Plesch, A. (2002). Shallow seismic imaging of folds above the Puente Hills blind-thrust fault, Los Angeles, California. Geophysical Research Letters, 29(9), 18-1–18-4. https://doi.org/10.1029/2001gl014313

Pratt, T. L. (2026). Seismic reflection profiles across the Puente Hills fault zone, Los Angeles, California. U.S. Geological Survey data release. https://doi.org/10.5066/10.5066/P1XIR92T

Prescott, J. R., & Hutton, J. T. (1994). Cosmic ray contributions to dose rates for luminescence and ESR dating. Radiation Measurements, 23(2-3), 497-500. https://doi.org/10.1016/1350-4487(94)90086-8

Ramsey, C. B. (1995). Radiocarbon calibration and analysis of stratigraphy: The OxCal program. Radiocarbon, 37(2), 425-430. https://doi.org/10.1017/S0033822200030903

Ramsey, C. B. (2001). Development of the radiocarbon calibration program. Radiocarbon, 43(2A), 355-363. https://doi.org/10.1017/S0033822200038212

Reichard, E. G., Crawford, S. M., Land, M. T., & Paybins, K. S. (1999). Management of groundwater supply and water quality in the Los Angeles Basin, California. In The 2nd International Symposium on Assessing and Managing Health Risks from Drinking Water Contamination: Approaches and Applications (No. 260, pp. 91-92).

Rhodes, E. J. (2011). Optically stimulated luminescence dating of sediments over the past 200,000 years. Annual Review of Earth and Planetary Sciences, 39(1), 461-488. https://doi.org/10.1146/annurev-earth-040610-133425

Rhodes, E. J. (2015). Dating sediments using potassium feldspar single-grain IRSL: initial methodological considerations. Quaternary International, 362, 14-22. https://doi.org/10.1016/j.quaint.2014.12.012

Rollins, C., Avouac, J. P., Landry, W., Argus, D. F., & Barbot, S. (2018). Interseismic strain accumulation on faults beneath Los Angeles, California. Journal of Geophysical Research: Solid Earth, 123(8), 7126-7150. https://doi.org/10.1029/2017JB015387

Shaw, J. H., Hook, S. C., & Suppe, J. (1994). Structural trend analysis by axial surface mapping. AAPG Bulletin, 78(5), 700-721. https://doi.org/10.1306/A25FE38D-171B-11D7-8645000102C1865D

Shaw, J. H., & Suppe, J. (1996). Earthquake hazards of active blind-thrust faults under the central Los Angeles basin, California. Journal of Geophysical Research: Solid Earth, 101(B4), 8623-8642. https://doi.org/10.1029/95JB03453

Shaw, J. H., & Shearer, A. P. M. (1999). An elusive blind-thrust fault beneath metropolitan Los Angeles. Science, 283(5407), 1516-1518. https://doi.org/10.1126/science.283.5407.1516

Shaw, J. H., Plesch, A., Dolan, J. F., Pratt, T. L., & Fiore, P. (2002). Puente hills blind-thrust system, Los Angeles, California. Bulletin of the Seismological Society of America, 92(8), 2946-2960. https://doi.org/10.1785/0120010291

Shaw, J. H., Novoa, E., & Connors, C. D. (2004). Structural controls on growth stratigraphy in contractional fault-related folds, in McClay, K. R., (ed.), Thrust tectonics and hydrocarbon systems: AAPG Memoir 82.

American Association of Petroleum Geologists: Tulsa, OK, pp. 400–412. https://archives.datapages.com/data/specpubs/memoir82/CHAPTER20/CHAPTER20.HTM

Shaw, J. H., Connors, C. D., & Suppe, J. (eds.) (2005). Seismic interpretation of contractional fault-related folds: An AAPG Seismic Atlas, Studies in Geology #53. American Association of Petroleum Geologists: Tulsa, OK, 156 pp. https://doi.org/10.1306/St531003

Stein, R. S., & King, G. C. (1984). Seismic potential revealed by surface folding: 1983 Coalinga, California, earthquake. Science, 224(4651), 869-872. https://doi.org/10.1126/science.224.4651.869

Suppe, J. (1983). Geometry and kinematics of fault-bend folding. American Journal of Science, 283(7), 684-721. https://doi.org/10.2475/ajs.283.7.684

Suppe, J., Chou, G. T., & Hook, S. C. (1992). Rates of folding and faulting determined from growth strata. In: McClay, K. R. (ed.) Thrust Tectonics. Springer Netherlands: Dordrecht, pp. 105-121. https://doi.org/10.1007/978-94-011-3066-0_9

Thomsen, K. J., Murray, A. S., Jain, M., & Bøtter-Jensen, L. (2008). Laboratory fading rates of various luminescence signals from feldspar-rich sediment extracts. Radiation Measurements, 43, 1474–1486. https://doi.org/10.1016/j.radmeas.2008.06.002

Tucker, A. Z., & Dolan, J. F. (2001). Paleoseismologic evidence for a> 8 ka age of the most recent surface rupture on the eastern Sierra Madre fault, northern Los Angeles metropolitan region, California. Bulletin of the Seismological Society of America, 91(2), 232-249. https://doi.org/10.1785/0120000093

Wallinga, J., Murray, A., & Wintle, A. (2000). The single-aliquot regenerative-dose (SAR) protocol applied to coarse-grain feldspar. Radiation Measurements, 32(5-6), 529-533. https://doi.org/10.1016/S1350-4487(00)00091-3

Walls, C., Rockwell, T., Mueller, K., Bock, Y., Williams, S., Pfanner, J., Dolan, J.F., & Fang, P. (1998). Escape tectonics in the Los Angeles metropolitan region and implications for seismic risk. Nature, 394(6691), 356-360. https://doi.org/10.1038/28590

Wolfe, F. D., Shaw, J. H., Plesch, A., Ponti, D. J., Dolan, J. F., & Legg, M. R. (2019). The Wilmington blind-thrust fault: An active concealed earthquake source beneath Los Angeles, California. Bulletin of the Seismological Society of America, 109(5), 1890-1906. https://doi.org/10.1785/0120180335

Woodring, W. P., Bramlette, M. N., & Kew, W. S. W. (1946). Geology and paleontology of Palos Verdes Hills, California. U.S. Geological Survey Professional Paper 207, 145 pp. https://doi.org/10.3133/pp207

Wright, T. L. (1991). Structural geology and tectonic evolution of the Los Angeles Basin, California. In: Biddle, K. T. (ed.) Active Margin Basins: AAPG Memoir 82, American Association of Petroleum Geologists: Tulsa, OK, pp. 35-134. https://doi.org/10.1306/M52531C3

Yerkes, R. F., McCulloh, T. H., Schoellhamer, J. E., & Vedder, J. G. (1965). Geology of the Los Angeles Basin California - An Introduction. U.S. Geological Survey Professional Paper 420, 57 pp., 4 plates. https://doi.org/10.3133/pp420A

Yielding, G., Jackson, J. A., King, G. C. P., Sinvhal, H., Vita-Finzi, C., & Wood, R. M. (1981). Relations between surface deformation, fault geometry, seismicity, and rupture characteristics during the El Asnam (Algeria) earthquake of 10 October 1980. Earth and Planetary Science Letters, 56, 287-304. https://doi.org/10.1016/0012-821X(81)90135-7

Zinke, R., Dolan, J. F., Rhodes, E. J., Van Dissen, R., & McGuire, C. P. (2017). Highly Variable Latest Pleistocene-Holocene Incremental Slip Rates on the Awatere Fault at Saxton River, South Island, New Zealand, Revealed by Lidar Mapping and Luminescence Dating. Geophysical Research Letters, 44(22), 11301-11310. https://doi.org/10.1002/2017GL075048

Zinke, R., Dolan, J. F., Rhodes, E. J., Van Dissen, R., McGuire, C. P., Hatem, A. E., et al. (2019). Multimillennial Incremental Slip Rate Variability of the Clarence Fault at the Tophouse Road Site, Marlborough Fault System, New Zealand. Geophysical Research Letters, 46(2), 717–725. https://doi.org/10.1029/2018GL080688

1083

9. Tables

Table 1. Structural relief and ages of marker horizons

	Forelimb Relief (m)			**Backlimb Relief (m)**				**Age (ka)**				
Sequence Top	Min	**Pref**	Max	Min	**Pref**	Max		**Pref**	Min	Max	**Age range determined from**	**Marine Isotope Stage**
Gaspur aquifer (Dominguez)	4.14	5.04	5.74	3.5	5.9	7.1		**10.1**	**9.15**	**10.67**	Leon et al. (2007) sample 2010 and sample 1813	Holocene
Mesa	7.5	10.6	13.7	10.4	13.4	16.4		**21.4**	**17**	**28**	Between the base of Dominguez and the Laschamp magnetic polarity event (~40 ka) identified in Long Beach holes. Preferred age from ^{14}C sample collected from the Pico Rivera hole. Oldest age boundary from luminescence dating in McDougall et al. (2012)	MIS 2, 3 and 4
Pacific	28.2	52.2	76.2	32.6	38.6	44.6		**110**	**80**	**117**	Between the oldest age of the Pacific A or the Pacific and the Blake magnetic polarity event at ~117 ka	MIS 5
Harbor	64.1	83.6	103.1	44.6	57.1	69.6		**160**	**117**	**200**	Between the Blake polarity event and the Pringle Falls magnetic event	MIS 6
upper Wilmington	103.9	127.9	151.9	77.6	88.6	99.6		**475**	**450**	**550**	Base of the Brent Spring sequence and the Big Lost magnetic event	MIS 13 to MIS 14
lower Wilmington	106.8	132.8	158.8	89.6	108.6	127.6		**580**	**580**	**640**	Base of the upper Wilmington and the age of the Lava Creek ash	MIS 17+ to MIS 15
upper Long Beach	163.8	189.8	215.8	125.6	164.6	203.6		**1400**	**780**	**1770**	Base of the lower Wilmington and the Olduvai Normal Polarity Subcrhon	

Table 2. Cumulative fault displacements of marker horizons

	Forelimb displacement (m)			**BL-S1 displacement (m)**			**BL-S2 displacement (m)**			Cumulative Displacement Ratios	
Sequence Top	Min	**Pref**	Max	Min	**Pref**	Max	Min	**Pref**	Max	FL : BL-S2	BL-S2 : BL-S1
Gaspur aquifer (Dominguez)	9.1	11.1	12.6	12.8	21.4	25.8	14.3	24.0	28.9	0.46	1.12
Mesa	16.4	23.3	30.1	37.5	48.4	59.2	42.0	54.2	66.3	0.43	1.12
Pacific	62.0	114.9	167.8	117.9	139.6	161.3	132.0	156.3	180.6	0.73	1.12
Harbor	141.2	184.1	227.1	161.3	206.5	251.7	180.6	231.3	281.9	0.80	1.12
upper Wilmington	228.8	281.7	334.6	280.7	320.5	360.3	314.4	358.9	403.5	0.78	1.12
lower Wilmington	235.3	292.6	349.8	324.1	392.9	461.6	363.0	440.0	517.0	0.66	1.12
upper Long Beach	360.8	418.1	475.4	454.4	595.5	736.6	508.9	667.0	825.0	0.63	1.12

Table 3. Slip rates for the three fault segments

	Time Span			Prefered Incremental Displacements (m)			Fault Ramp Segment Slip Rates									Slip Rate Ratios (FBSRR)	
							Forelimb			BL-S1			BL-S2				
Sequences	**~From (ka)**	**~To (ka)**	**Delta (ka)**	**FLR**	**BLR-S1**	**BLR-S2**	**Rate (mm/yr)**	**+**	**-**	**Rate (mm/yr)**	**+**	**-**	**Rate (mm/yr)**	**+**	**-**	**FL : BL-S2**	**BL-S2 : BL-S1**
Top Gaspur to Present	10.1	0	10.1	11.1	21.4	24.0	**1.11**	0.09	0.09	**2.15**	0.24	0.23	**2.41**	0.26	0.26	0.46	1.12
Top Mesa to Top Gaspur	21.4	10.1	11.3	12.2	27.0	30.2	**1**	0.41	0.32	**2.23**	0.79	0.60	**2.50**	0.88	0.67	0.40	1.12
Top Pacific to Top Mesa	110	21.4	88.6	114.9	139.6	156.3	**1.14**	0.36	0.34	**1.13**	0.23	0.18	**1.27**	0.25	0.2	0.90	1.12
Top Harbor to Top Pacific	160	110	50	69.3	66.9	75.0	**1.23**	1	0.62	**1.18**	0.88	0.50	**1.32**	0.98	0.56	0.93	1.12
Top upper Wilmington to Top Harbor	475	160	315	281.7	320.5	358.9	**0.26**	0.1	0.09	**0.34**	0.10	0.09	**0.38**	0.11	0.1	0.68	1.12
Top lower Wilmington to Top upper Wilmington	580	475	105	10.9	72.4	81.1	**0.28**	0.32	0.2	**0.68**	0.47	0.35	**0.77**	0.52	0.39	0.36	1.13
Top upper Long Beach to Top lower Wilmington	1400	580	820	418.1	595.5	667.0	**0.16**	0.1	0.06	**0.28**	0.19	0.12	**0.31**	0.21	0.13	0.52	1.11

10. Figures

Figure captions are retained in main text.

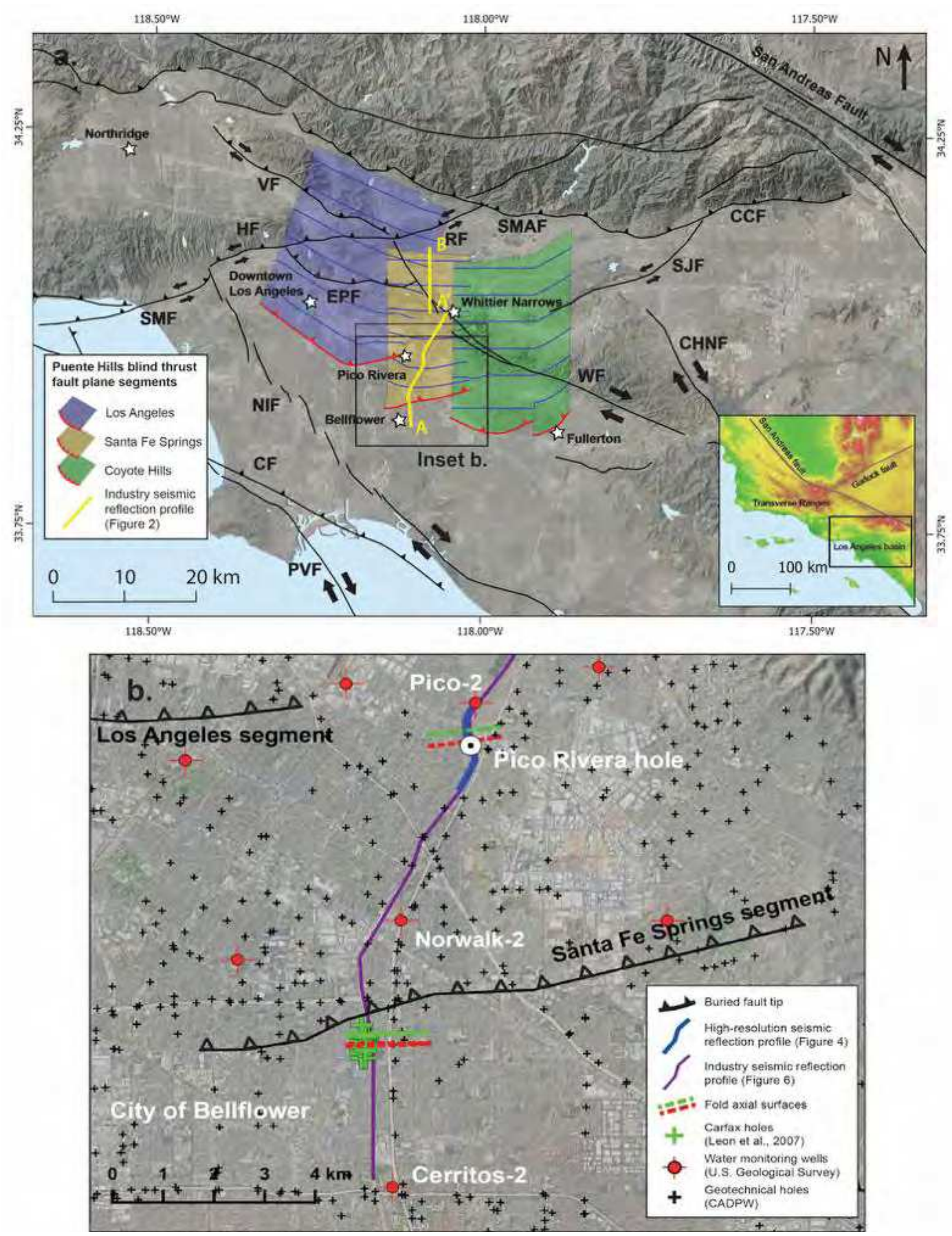

Figure 1.

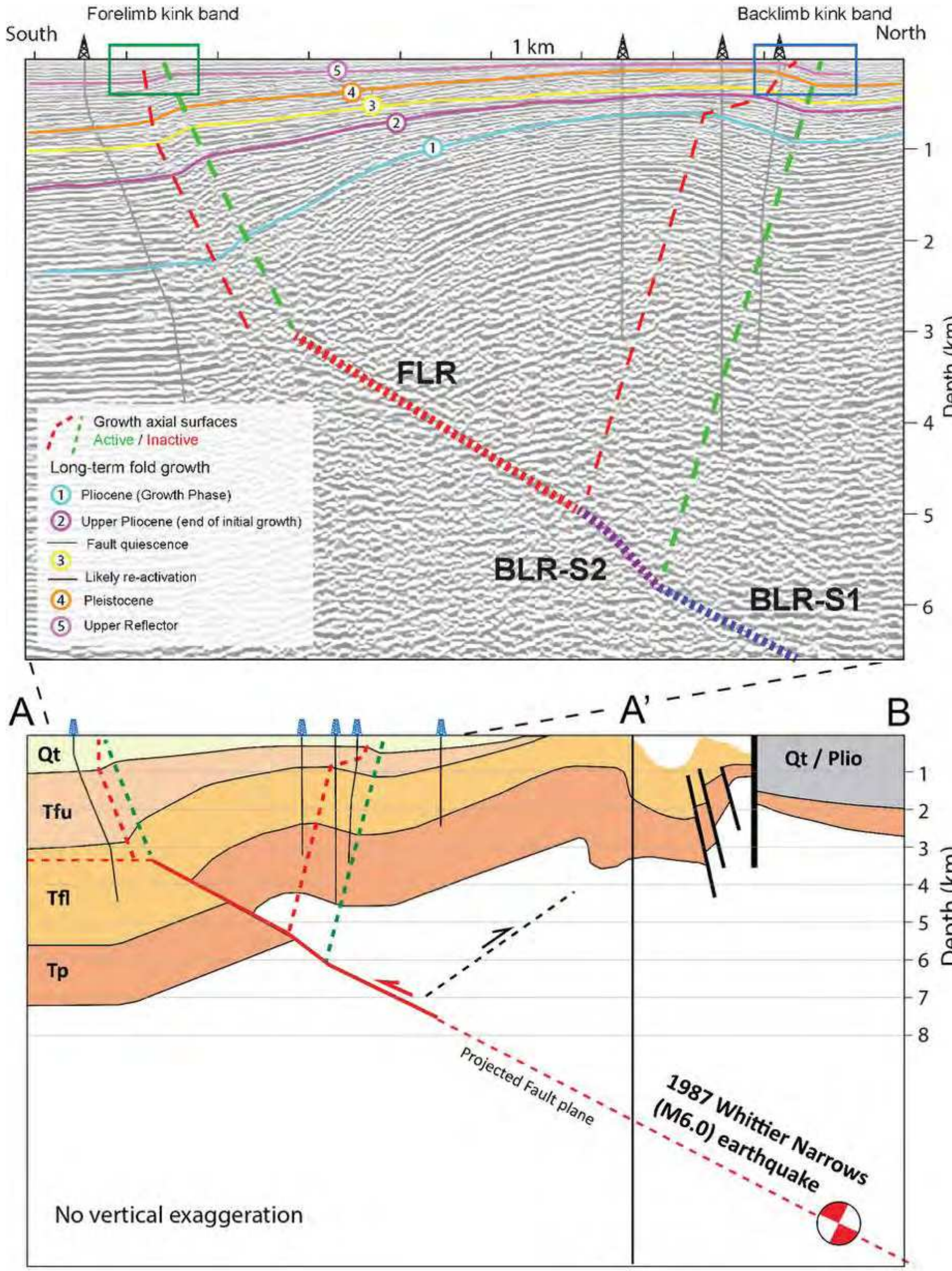
Forelimb kink band
Backlimb kink band
South
North
1 km
5
4
3
2
1
FLR
BLR-S2
BLR-S1
Depth (km)
Growth axial surfaces
Active / Inactive
Long-term fold growth
1 Pliocene (Growth Phase)
2 Upper Pliocene (end of initial growth)
Fault quiescence
3
Likely re-activation
4 Pleistocene
5 Upper Reflector
A
A'
B
Qt
Tfu
Tfl
Tp
Qt / Plio
Projected Fault plane
1987 Whittier Narrows (M6.0) earthquake
No vertical exaggeration

Figure 2.

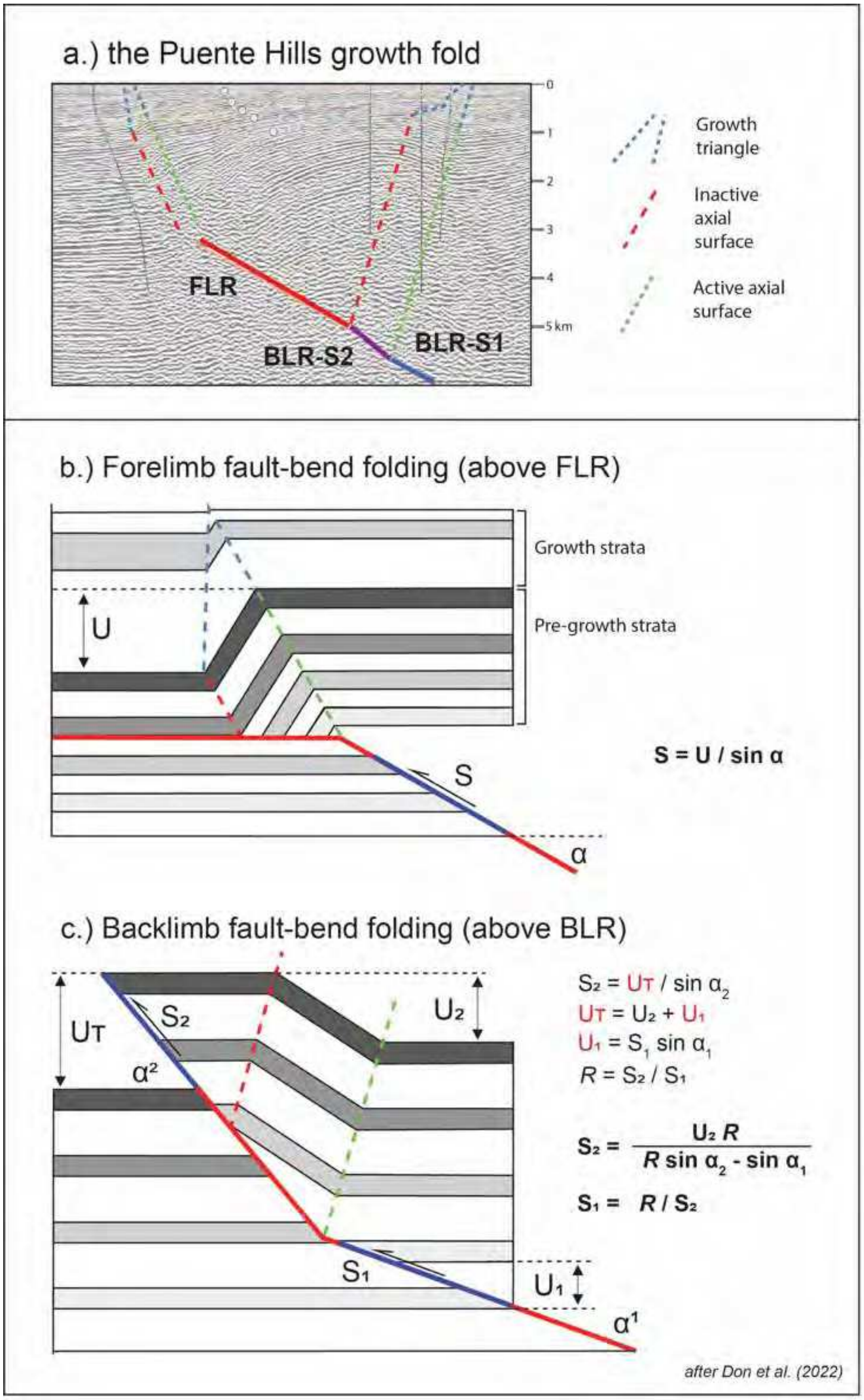

a.) the Puente Hills growth fold
0
1
2
3
4
5 km
FLR
BLR-S2
BLR-S1
Growth triangle
Inactive axial surface
Active axial surface
b.) Forelimb fault-bend folding (above FLR)
Growth strata
Pre-growth strata
U
S
α
S = U / sin α
c.) Backlimb fault-bend folding (above BLR)
UT
S2
α2
U2
S1
U1
α1
S2 = UT / sin α2
UT = U2 + U1
U1 = S1 sin α1
R = S2 / S1
S2 = U2 R / (R sin α2 - sin α1)
S1 = R / S2
after Don et al. (2022)

Figure 3.

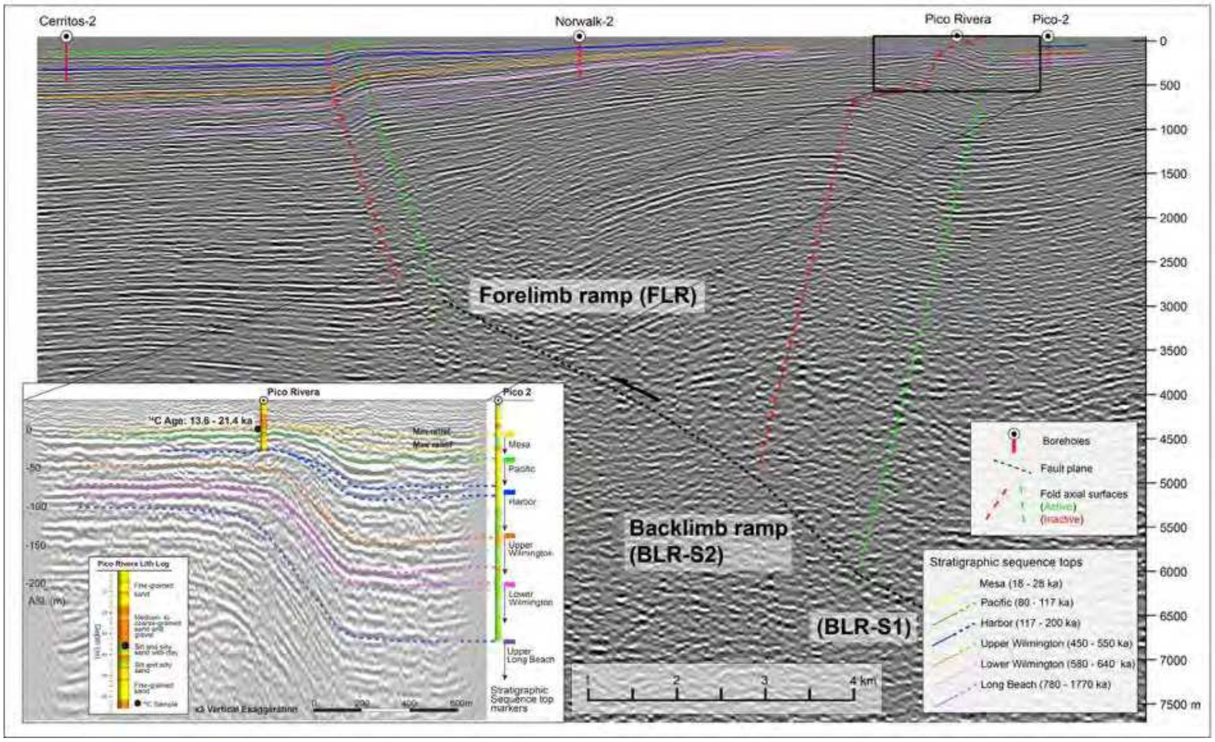

Figure 4.

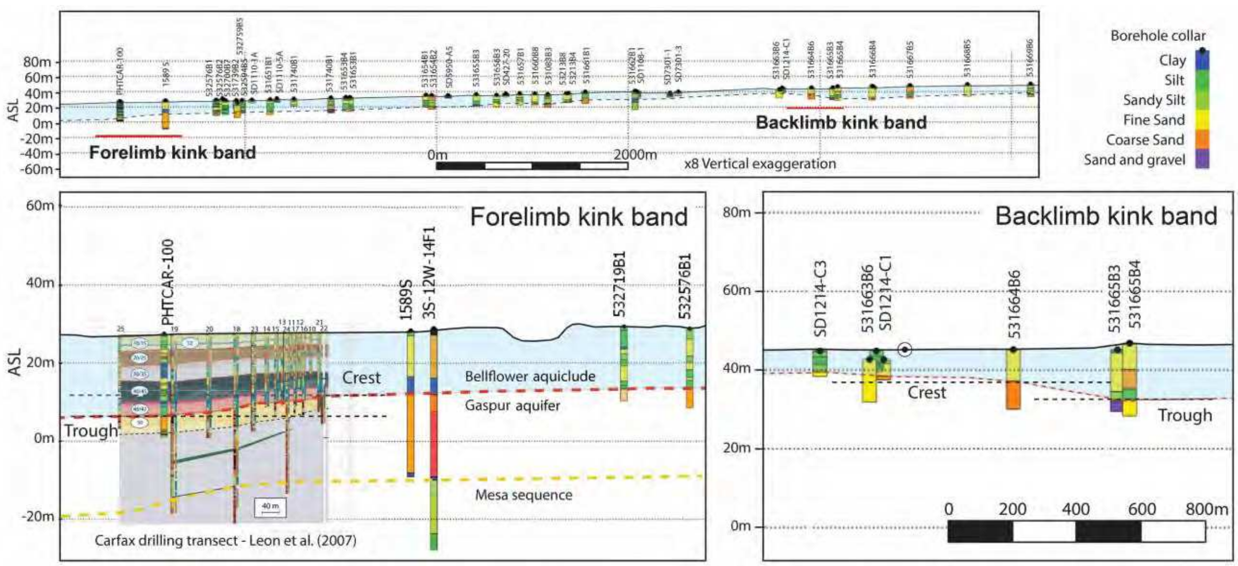

Figure 5.

1109

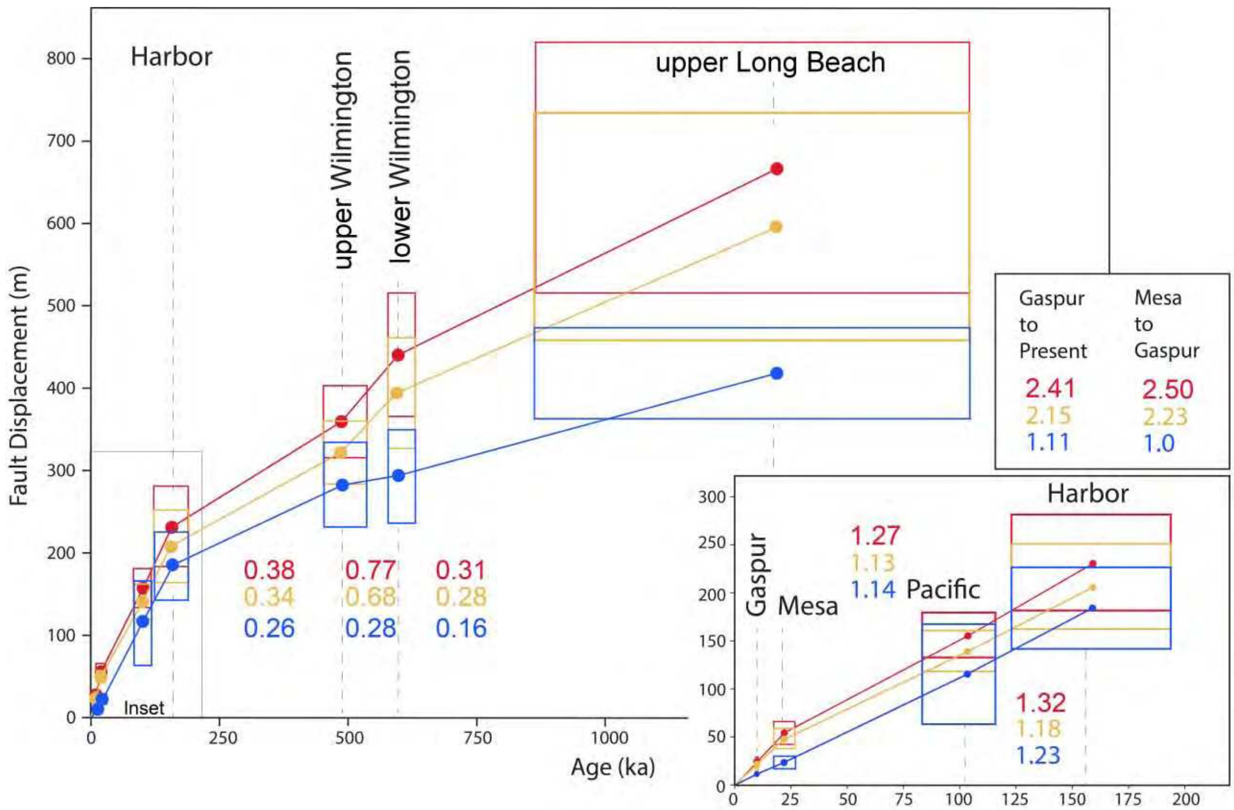

1110

1111 ***Figure 6.***